Ph.D. DISSERTATION

Inducing reversible polarization switching in HfO_2-ZrO_2 thin films for energy and memory applications

by

Keum Do Kim

August 2019

DEPARTMENT OF MATERIALS SCIENCE AND ENGINEERING

COLLEGE OF ENGINEERING

SEOUL NATIONAL UNIVERSITY

Inducing reversible polarization switching in HfO_2-ZrO_2 thin films for energy and memory applications

Advisor: Prof. Cheol Seong Hwang

by

Keum Do Kim

A thesis submitted to the Graduate Faculty of Seoul National University in partial fulfillment of the requirements for the Degree of Doctor of Philosophy

Department of Materials Science and Engineering

August 2019

Approved

by

Chairman of advisory Committee:	SangBum Kim
Vice-chairman of Advisory Committee:	Cheol Seong Hwang
Advisory Committee:	Seungwu Han
Advisory Committee:	Min Hyuk Park
Advisory Committee:	Yu Jin Kim

Abstract

Ferroelectricity and field-induced ferroelectricity in doped HfO_2 and HfO_2-ZrO_2 solid solution films have been studied since the ferroelectricity in HfO_2 thin film was first reported in 2011. The significant merits for the utilization in future semiconductor devices could be found in such thin films, such as large electrical band gap (~5.5eV) and Si-compatibility, compared to the conventional perovskite-based ferroelectric thin films. However, the previous reports mainly focused on the ferroelectric properties based on irreversible polarization switching at the metal-ferroelectric-metal (MIM) or metal-ferroelectric-(insulator)-semiconductor structures and the related nonvolatile memory aspects, but the reversible polarization switching properties induced in the HfO_2–ZrO_2 thin film at the optimized processes were not studied in detail. Contrary to the irreversible polarization switching operation observed in conventional MFM capacitor, the reversible polarization switching specifically means the switching behavior where the switched polarization by the action of external electric field shows the reversible back-switching when the electric field is removed. The ferroelectric layer which shows this type of polarization switching can be hardly used as nonvolatile memory device because it cannot retain any memory state in absence of external voltage, but the large capacitance change induced by the P_s reversal facilitates the utilization in energy storage and negative capacitance devices in combination with the promising electrical and physical properties of HfO_2-ZrO_2 thin film. Therefore,

this work presents the reversible polarization switching in HfO_2-ZrO_2 thin films induced by two different methods in chapter 3 and 4.

The first method presented in chapter 3 uses the stabilization of nonpolar tetragonal phase, where the study was carried out for the potential application of the MFM capacitor in electrostatic energy storage device. When the tetragonal phase is stabilized in HfO_2-ZrO_2 thin films, the electric field-induced reversible phase transition to polar orthorhombic phase can be possible due to the structural similarity between them. It facilitates the double-hysteresis curve in P-E diagram with large P_{max} and low P_r, which is beneficial characteristic for electrostatic supercapacitor device. However, to date, the high energy storage performances observed in the field-induced ferroelectric HfO_2- or ZrO_2-based films have had an obstacle to scale-up due to the involvement of low-k monoclinic phase at the large thickness (> ~10 nm). Considering that the monoclinic phase formation is closely related with the in-situ (partial) crystallization during the atomic layer deposition (ALD) process, in this chapter, the ALD temperature of $Hf_{0.5}Zr_{0.5}O_2$ thin films was lowered, and its influence on the energy storage performances was systematically examined. Carbon and nitrogen dopants incorporated at a low deposition temperature in combination with grain size decrease change the polymorphism of $Hf_{0.5}Zr_{0.5}O_2$ thin film from the genuine ferroelectric to field induced (incipient) ferroelectric crystal structure. The $Hf_{0.5}Zr_{0.5}O_2$ thin film deposited at 210 °C shows improved resistance to degradation by monoclinic phase involvement up to ~ 40 nm compared to the previously-reported $Hf_{0.3}Zr_{0.7}O_2$ thin films.

The second method presented in chapter 4 uses the induction of depolarization field by inserting dielectric layer between ferroelectric and electrode layers. Due to the negative capacitance effect of ferroelectric material, the ferroelectric/dielectric bilayer capacitance density observed during the reversible polarization switching can be larger than the capacitance density of the constituent dielectric layer in the bilayer structure. This phenomenon is called capacitance boosting by (transient) negative capacitance effect, and now attracting a great deal of attention in work towards low-power operation of field effect transistors and extremely large capacitance density in dynamic random access memory. However, to date, observation of the NC effect in dielectric/ferroelectric bilayer capacitors has been limited to the use of epitaxial ferroelectric thin films based on perovskite crystal structures, such as $Pb(Zr,Ti)O_3$ and $BaTiO_3$, which is not compatible with current complementary metal oxide semiconductor technology. This chapter, therefore, reports on the transient NC effect in amorphous-Al_2O_3/polycrystalline-$Hf_{0.3}Zr_{0.7}O_2$ bilayer systems prepared using atomic layer deposition. The thin film processing conditions are carefully tuned to achieve the appropriate ferroelectric performances that are a prerequisite for the examination of the transient NC effect. Capacitance enhancement is observed in a wide voltage range in 5–10 nm thick $Al_2O_3/Hf_{0.3}Zr_{0.7}O_2$ bilayer thin films. It is found that the capacitance of the dielectric layer plays critical role in the determination of additional charge density induced by the NC effect. In addition, inhibition of the leakage current is important for stabilization of nonhysteretic charge–discharge

behavior of the bilayers. The mean-field approximation combined with classical Landau formalism precisely reproduces the experimental results.

Keywords: ferroelectric material, HfO_2-ZrO_2 thin film, electrostatic supercapacitor, energy storage, capacitance boosting, negative capacitance, reversible polarization switching

Student Number: 2014-21482

Table of Contents

[1] Keum Do Kim, Yu Jin Kim, Min Hyuk Park, Hyeon Woo Park, Young Jae Kwon, Yong Bin Lee, Han Joon Kim, Taehwan Moon, Young Hwan Lee, Seung Dam Hyun, Baek Su Kim, and Cheol Seong Hwang*, *Advanced Functional Materials*, 1808228 (2019)

[2] Keum Do Kim, Young Hwan Lee, Taehong Gwon, Yu Jin Kim, Han Joon Kim, Taehwan Moon, Seung Dam Hyun, Hyeon Woo Park, Min Hyuk Park*, Cheol Seong Hwang*, *Nano Energy*, 39, 390-399 (2017)

[3] Keum Do Kim, Min Hyuk Park, Han Joon Kim, Yu Jin Kim, Taehwan Moon, Young Hwan Lee, Seung Dam Hyun, Taehong Gwon, and Cheol Seong Hwang*, *Journal of Materials Chemistry C*, 4, 6864-6872 (2016)

List of Tables

List of Figures

1. Introduction

1.1. Ferroelectric HfO_2 thin films and the issues

The ferroelectricity of doped HfO_2 films was first reported by Boescke et al. in 2011 [1]. The crystal structure showing ferroelectricity in HfO_2 has been confirmed as a non-centrosymmetric orthorhombic crystal structure (space group $Pca2_1$) [2]. The Figure 1.1 shows two polar states in the ferroelectric crystal structure of HfO_2, where the red sphere represents oxygen ion, and the blue sphere represents hafnium ion. The formation of spontaneous dipole by the movement of four oxygen ions in the left can be observed. The magnitude of spontaneous polarization reported in the first principle calculation is ~50 $\mu C/cm^2$ [3,4]. The ferroelectric thin film based on the existing perovskite crystal structure can exhibit ferroelectricity at a thickness of >~50 nm, however the doped HfO_2 thin film can exhibit excellent ferroelectricity even at ~10 nm due to a large band gap of ~ 5.5 eV. The coercive field is ~0.8-1.2 MV/cm, which is one order larger than the perovskite ferroelectric thin film of ~0.1 MV/cm, and the remanent polarization reaches ~ 10-45 $\mu C/cm^2$ depending on the type of dopant [5]. These doped HfO_2 can easily form an orthorhombic phase in TiN and TaN electrodes, also can be deposited using ALD, so it has no Si compatibility issue. In particular, HfO_2-ZrO_2 thin film is promising due to the fact that it can form a solid solution in the entire dopant concentration range, therefore it typically shows excellent reproducibility even though a certain fluctuation in dopant concentration exists, and can crystallize at a low temperature of 400-600 ^oC.

In ferroelectric HfO_2 thin films, the issues related with the formation of the ferroelectric orthorhombic phase have been considered critical for the integration of such material into the memory and energy devices. Since the polar orthorhombic phase is a metastable phase that does not appear in the bulk phase diagram of HfO_2 in bulk state, the ferroelectric properties of the thin film can hardly be maintained stable, and the electrical properties can change depending on the detailed changes in the thin film processing. Previous studies have shown that the specific thermodynamic effects that occur during the formation of thin films play an important role in stabilizing the phases on the thin film [5,6]. Among them, doping, such as Zr element, interface/grain boundary energy, and top encapsulation effects are considered to be critical [6].

Generally, the best ferroelectric properties of doped HfO_2 thin films are observed in the thickness of ~10 nm. On the other hand, it was reported that the remanent polarization was shown to change when the thickness of the thin film deviates from ~10 nm because the grain size changes depending on the film thickness, and thus the surface-to-volume ratio affecting on each grain changes. The room-temperature stable monoclinic phase in HfO_2 and ZrO_2 materials can be destabilized by the surface/grain boundary energy contribution owing to the smaller surface energy of other high-k phases than monoclinic phase [5]. Conversely, when the film thickness is increased from >~10 nm, the monoclinic phase fraction gradually increases in the thin film, and the corresponding deterioration of the electrical characteristics, such as remanent polarization and dielectric constant, occurs. This monoclinic phase

involvement at large thickness is considered a critical obstacle in energy applications of ferroelectric HfO_2, such as electrocaloric cooling, energy harvesting, and electrostatic supercapacitors [7].

Since the heat treatment during the ALD process is not enough to fully crystallize the thin film, it stays almost in an amorphous state in the as-deposited state. It is another important issue that certain additional crystallization heat treatment is required. Si-doped HfO_2 thin films need the high crystallization temperature of 800-1000 ^oC [5]. The crystallization temperature of HfO_2-ZrO_2 thin films is relatively low at 400-600 ^oC, nevertheless it may cause significant failure when the thermal budget of the integrated system is lower than it. In addition, the phase stabilized on the thin film can be changed according to the crystallization conditions, such as post-metallization annealing (PMA) or post-deposition annealing (PDA). It was known that the top encapsulation effect inhibits the formation of the monoclinic phase when it is crystallized in the PMA condition, whereas the crystallization in the PDA condition can increase the monoclinic phase fraction in the thin film, and reduces the ferroelectric response [1]. Therefore, since the ferroelectric phase of HfO_2 thin film is sensitive to the process conditions, it is necessary to precisely control the process conditions according to the potential applications.

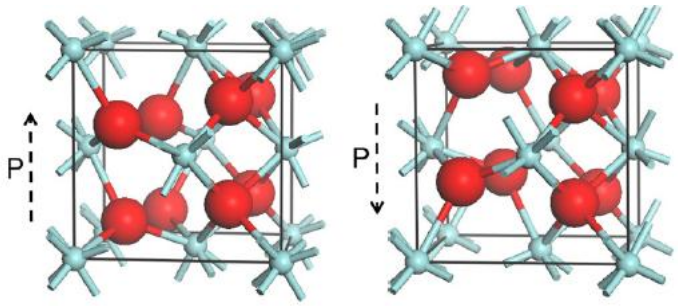

Figure 1.1 Polar orthorhombic structure of HfO_2 material (space group $Pca2_1$). The spontaneous dipole direction is indicated by black arrows. The red spheres are oxygen ions, and blue spheres are hafnium ions [1].

1.2. Polarization switching operation and device applications

Device applications of ferroelectric thin films can be classified according to the polarization switching operation. When the external voltage is applied on a ferroelectric thin film in a MFM (metal-ferroelectric-metal) capacitor in the opposite direction to the P_s, it can be reversed in the external voltage direction. The P_s can maintain the switched state even after the applied voltage is subsequently removed because the bound charge compensates the electric dipole of the switched polarization, which then can be electostatically stabilized. This process can be called specifically as irreversible polarization switching. It is well known that this characteristic of ferroelectric thin film could be used as nonvolatile memory devices [8]. Ferroelectric random access memory (FeRAM), one of the representative nonvolatile memories using ferroelectric materials, can distinguish 0 and 1 by sensing (non-) switched current when a read voltage is applied to the MFM capacitor. As can be seen in the upper panel of Figure 1.2, the maximum memory window of MFM capacitor is $2P_r$. In the ferroelectric-field effect transistor (FeFET), the channel current can be changed by controlling the potential of the channel region when the bound charge of the ferroelectric layer located at the gate oxide position of the MOSFET (metal-oxide-semiconductor field effect transistor) is switched. There can be other application that uses polarization state of ferroelectric layer, such as tristate memory [9].

In contrast, the P_s of ferroelectric material can be reversibly back-switched when the external voltage is removed when the factors related with the formation or

switching of P_s in the thin film is controlled. This operation specifically can be called reversible polarization switching. During such an operation, the electric capacitance change induced by the reversible motion of P_s can be exploited. However, to date, the researches on the reversible polarization switching of ferroelectric HfO_2 thin film and the related applications have not been carried out systematically. In ferroelectric HfO_2 thin films, the operation can be implemented by increasing the stability of the tetragonal phase, which is a paraelectric (nonpolar) phase, or by inducing the depolarization field by stacking a dielectric layer. The tetragonal crystal structure of HfO_2 and ZrO_2 is a nonpolar paraelectric phase corresponding to the polar orthorhombic phase, and is known to show the (first-order) field-induced phase transition between them [4]. Such field-induced phase transition can be observed in $(Hf,Zr)O_2$ thin film, Si-doped HfO_2 thin film, and Al-doped HfO_2 thin film especially at the doping concentrations above the optimal ferroelectric properties [5]. As shown in the center panel of Figure 1.2, the field-induced phase transition appears as a double-hysteresis in the P-V curve, which is similar to the behavior of a typical antiferroelectric material. However, it should be noted that there is no anti-parallel dipole in the crystal structure, but the reversible phase transition between t-phase and o-phase is responsible for such hysteresis. It is known that the nonlinear capacitors showing the spontaneous polarization can store a larger amount of electrical energy than a linear dielectric capacitors owing to its larger polarizability [10]. In addition, the thin films exhibiting field-induced ferroelectricity are considered more promising in energy storage applications due to the lower P_r, thereby obtaining a larger recoverable energy density (described in detail in Section 2.1).

When a metal-insulator-ferroelectric-metal (MIFM) structure is formed by stacking dielectric layer between ferroelectric and electrode layers, the depolarization field can be induced in the ferroelectric layer because the distance between the switched polarization and the bound charge in the electrode is increased. The bottom panel of Figure 1.2 shows the spontaneous polarization of the ferroelectric layer imprinted upward direction in the initial state. If the thickness of the dielectric layer is sufficiently thin, the depolarization field may be small even after the polarization is switched, then the switched polarization can stay in the switched state. This case is similar to the situation observed in a MFM capacitor where the certain thickness of dead layer is formed. On the other hand, if the thickness of the dielectric layer is thick enough, the bound charge can not electrostatically stabilize the spontaneous dipole, and the depolarization field reversibly return the switched polarization to the initial state. It was known that the discharge density flowing out of the capacitor can be larger than the electric charge corresponding to the capacitance of the single constituent dielectric layer of the bilayer owing to the characteristic negative capacitance effect of the ferroelectric material (described in detail in Section 2.2) [11]. The capacitance boosting due to negative capacitance effect is widely studied for negative capacitance-field effect transistor (NC-FET) or a next-generation dynamic random access memory (DRAM) capacitor.

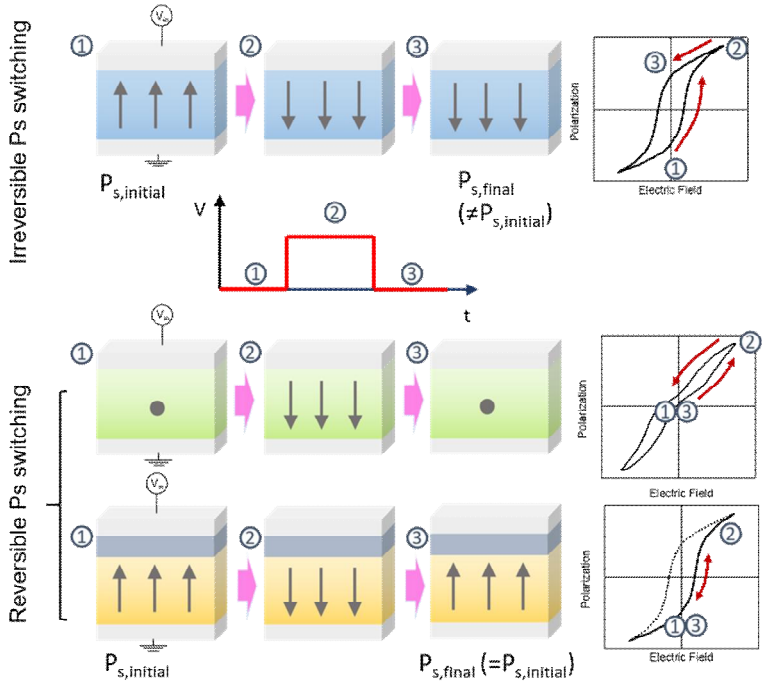

Figure 1.2 The irreversible and reversible polarization switching of ferroelectric material and the corresponding P-V diagram. In irreversible polarization switching operation, the switched polarization remains the switched state after external voltage is removed (upper panel). In reversible polarization switching operation, the switched polarization reversibly back-switchs to the initial state after external voltage is removed (center and bottom panel).

1.3. Objective and chapter overview

Ferroelectric doped-HfO_2 and HfO_2-ZrO_2 thin films have been extensively studied recently in related with the application of the nonvolatile memory devices. However, the reversible polarization switching behavior and the related energy and memory applications of the thin films have not been investigated in detail although such material can exhibit outstanding performances. However, since the ferroelectric phase in HfO_2 and ZrO_2 materials is not a room-temperature stable phase, but a metastable phase, the ferroelectricity may change or even disappear depending on the process conditions or in the specific systems required in several applications. Therefore, the thin film processing conditions need to be carefully tuned to achieve the required ferroelectric (or field-induced ferroelectric) phase in the specific systems. In this dissertation, we have studied the induction of reversible polarization switching in thin films for the purpose of energy storage and negative capacitance phenomena of HfO_2-ZrO_2 thin films.

Chapter 3 presents the improvement on the characteristic degradation of HfO_2-ZrO_2 thin films at the large thickness. When the film thickness at >~10nm, the HfO_2-ZrO_2 thin film shows a decrease in the field-induced ferroelectric response due to an increase in the low-k monoclinic phase fraction. This is an obstacle to increasing the energy storage quantity through the scale-up of the thin film. The formation of a monoclinic phase at a large thickness is considered closely related with the insitu-crystallization phenomenon during the ALD process, and the achieving the field-

induced ferroelectricity at the thin film deposited at the low temperature was studied for the improvement the energy storage characteristics at a large thickness. At the low deposition temperatures, it was found that the tetragonal phase can be stabilized by the effect of carbon and nitrogen doping in combination with slight grain size reduction in $Hf_{0.5}Zr_{0.5}O_2$ films, and the field-induced ferroelectricity by reversible polarization switching could be obtained. The field-induced ferroelectric $Hf_{0.5}Zr_{0.5}O_2$ deposited at 210 ºC showed improved resistance to degradation due to monoclinic phase formation at a large thickness than that of the conventional $Hf_{0.3}Zr_{0.7}O_2$ deposited at 280 ºC. The energy storage density of ~ 35 J/cm^3 in the film thickness of ~40 nm was obtained. This is the highest energy storage density obtained at the thickness among the ferroelectric HfO_2 thin film.

Chapter 4 covers the transient negative capacitance and the corresponding capacitance boosting phenomenon by inserting an Al_2O_3 (dielectric) layer in the HfO_2-ZrO_2 thin film. It was shown that the highly insulating properties of the dielectric layer are essential for the observation of the transient NC phenomenon because the internal field acting on the dielectric layer induces the injection of bound charge injection at the electrode. However, the conventional PMA condition for the crystallization of HfO_2-ZrO_2 thin film permitted the fluent movement of bound charge through the Al_2O_3 layer, therefore the PDA condition was adopted instead. In this condition, a slightly increased Zr content in HfO_2-ZrO_2 was required to inhibit the monoclinic phase formation in the thin film, and the absence of top encapsulation layer facilitated the crystallization toward ferroelectric orthorhombic phase rather

than tetragonal phase in $Hf_{0.3}Zr_{0.7}O_2$ thin film. The capacitance enhancement due to the reversible motion of Ps was observed over a wide voltage range in bilayer capacitors stacked with 5-10 nm Al_2O_3 layers. The mean-field approximation using classical landau formalism was used to explain the experimental results.

Finally, chapter 5 presents the conclusion of the dissertation.

1.4. Bibliography

[1] T. S. Boescke, J. Mueller, D. Braeuhaus, U. Schroeder, and U. Boettger, *Appl. Phys. Lett.*, 99, 102903 (2011).

[2] X. Sang, E. D. Grimley, T. Schenk, U. Schröder, J.M. LeBeau, *Appl. Phys. Lett.,* 106, 162905 (2015).

[3] R. Materlik, C. Künneth, A. Kersch, *Appl. Phys. Lett.,* 117, 134109 (2015).

[4] S. E. Reyes-Lillo, K. F. Garrity, K. M. Rabe, *Phys. Rev. B*, 90, 140103 (2014).

[5] M. H. Park, Y. H. Lee, H. J. Kim, Y. J. Kim, T. Moon, K. D. Kim, J. Mueller, A. Kersch, U. Schroeder, T. Mikolajick and C. S. Hwang, *Adv. Mater.*, 27, 1811 (2015)

[6] M. H. Park, Y. H. Lee, H. J. Kim, T. Schenk, W. Lee, K. D. Kim, F. P. G. Fengler, T. Mikolajick, U. Schroeder, and C. S. Hwang, *Nanoscale*, 9, 9973 (2017).

[7] M. H. Park, H. J. Kim, Y. J. Kim, T. Moon, K. D. Kim, C. S. Hwang, *Adv. Energy Mater.*, 4, 1400610 (2014).

[8] K. M. Rabe, C. H. Ahn, J.-M. Triscone, *Physics of Ferroelectrics: A Modern Perspective*, Springer, New York, (2007).

[9] M. H. Park, H. J. Lee, G. H. Kim, Y. J. Kim, J. H. Kim, J. H. Lee, and C. S. Hwang, *Adv. Funct. Mater.*, 21, 4305, (2011).

[10] I. Burn and D. M. Smyth, *J. Mater. Sci.*, 7, 339 (1972)

[11] A. I. Khan, D. Bhowmik, P. Yu, S. J. Kim, X. Pan, R. Ramesh, S. Salahuddin, *Appl. Phys. Lett.*, 99, 113501 (2011).

2. Literature

2.1. Electrostatic supercapacitor device

The electrostatic supercapacitors using nonlinear dielectric capacitors in solid-state energy storage technology now attracts increasing interest because they can exhibit higher power densities than the existing conventional Li-ion batteries or than the next-generation electrochemical supercapacitors owing to the fast (dis-) charging speeds of several ~μs [1]. On the other hand, the electrostatic supercapacitors usually exhibit lower energy storage densities (ESD) compared to other methods, for example, the electrochemical supercapacitors generally shows 1-2 order of higher ESD than the electrostatic supercapacitors, which is known that the biggest obstacle for the commerciallization of the electrostatic supercapacitor. Therefore, the hybrid energy storage system consisted of electrostatic supercapacitor at the front and electrochemical at the backward have been suggested, where the electrostatic supercapacitor were designed to capture the electrical energy from renewable energy source promptly, and the electrochemical supercapacitor stores the harvested energy [2]. Also, several 3D nanostructures for the increase of the ESD per projected area, such as Si nanotrench or the anodized aluminum oxide, were previously reported [3]. However, even in the 3D nanostructures, the thickness ratio between electrode layer and dielectric layer is considered important for the increase of maximum energy storage quantity [3], therefore the dielectric thickness needs to be larger compared to the electrode thickness. It was reported that the recoverable energy density can be significantly increased when the antiferroelectric polarization switching observed in

the several thin films is exploited due to the large polarizability and low P_r. [1]. The ESD in the thin films with nonlinear electric response can be expressed as the following equation.

$$W = \int EdP \tag{2.1}$$

The equation (2.1) indicates the electric work done on a capacitor by external power source when the electric field required for changing the polarization is dependent on the polarization, as in the case for ferroelectric or antiferroelectric capacitor. Figure 2.1(a) depicts the energy storage density in the (+) voltage region of the P-E curve [4]. The blue area represents ESD (recoverable energy density), and the green area represents the energy loss due to the polarization switching dynamics. The efficiency of electrostatic supercapacitor then can be defined as following equation.

$$\text{Efficiency} = \frac{\text{ESD}}{\text{ESD+Loss}} \tag{2.2}$$

Various perovskite-based (anti-) ferroelectric bulk ceramics or thin films previously have been studied for this application, and the ESD of a few of J/cm^3 were reported for bulk ceramics, and tens of J/cm^3 were reported for thin films. However, the use of lead for the PZT material among the thin films can be restricted in many countries due to the environmental impact. The linear dielectric polymers with low dielectric constant generally shows 1-2 J/cm^3 [1]. The fluorite-based ferroelectric material have shown the ESD up to ~61 J/cm^3 [5]. Thermal stability and cyclic endurance (bipolar or unipolar conditions) is the common endurance tests for the

electrostatic supercapacitor because the potential environments applied for the energy storage system usually require the large repetitive operation over a temperature range from ~ -100ºC to ~200ºC.

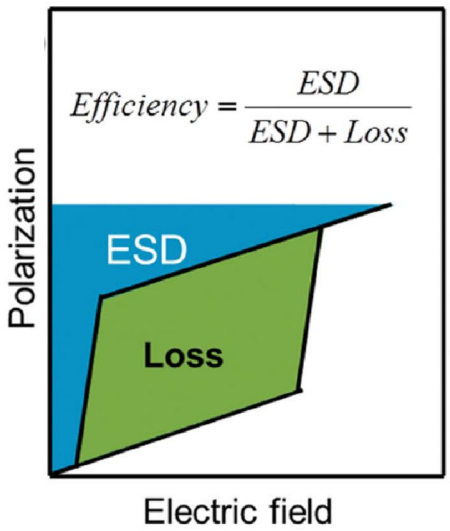

Figure 2.1 Schematic diagram for the energy storage behavior of nonlinear dielectric capacitors [4].

2.2. Negative capacitance device

The NC phenomenon was originally proposed to facilitate a very low voltage operation of the MOSFET device [6]. The external voltage applied to the gate of the MOSFET is divided into the gate oxide and the channel region according to the respective capacitance ratio. In this case, the theoretical minimum of the subthreshold swing, which means the gate voltage required to change the channel current ten times, is 60 mV/dec at room temperature as shown in Figure 2.2 [7]. However, when the ferroelectric layer in the gate oxide region can exhibit negative value of capacitance, the gate voltage can be amplified and the corresponding subthreshold swing can be decreased down to 60 mV/dec, which facilitates steep ON/OFF operation of MOSFET with low operation voltage (Figure 2.3) [8].

The negative capacitance effect in a ferroelectric material was predicted by the region near the P_s~0 in the free energy diagram depending on the P_s [6].

$$F_{f,0} = \frac{1}{2}\alpha P_s^2 + \frac{1}{4}\beta P_s^4 + \frac{1}{6}\gamma P_s^6$$

The free energy of ferroelectric material without the external electric field can be expressed by the above equation with P_s as an order parameter. The double-well potential shown in Figure 2.4 shows the free energy of general ferroelectric material. Since the reciprocal of the second differentiation of free energy with the P_s is proportional to the capacitance density, the negative capacitance can be expected at around P_s~0. However, in a ferroelectric material in a single layer, the P_s can hardly

retain the unpoled state, and is automatically separated into a stable ± Ps state. Meanwhile, it was proposed that when the dielectric layer, which has a single well potential in free energy diagram, is stacked with the ferroelectric layer, and the electrostatic coupling occurs in the two layers, the P_s~0 region of the ferroelectric layer can be stabilized as shown in Figure 2.4 [9]. Several experimental evidences on the capacitance boosting due to the occurrence of negative capacitance effect in such bilayer capacitors were reported in PZT/STO and BTO/STO capacitors [8,9].

$$\frac{1}{C_{tot}} = \frac{1}{C_{FE}} + \frac{1}{C_{DE}}$$

When the ferroelectric layer is in a negative capacitance state, the total capacitance can be larger than the capacitance of the single DE constituent layer. Therefore, by comparing the capacitance of the bilayer capacitor with the capacitance of the DE single layer, it can be experimentally demonstrated that the ferroelectric layer is in a negative capacitance state .

Unlike to perovskite-based thin films, such as PZT, BTO, and STO, the so-called electrostatic coupling state could not be observed in the general bilayer capacitors which have structurally dissimilar interface between ferroelectric and dielectric layers. It was found that the occurrence of interface trap charge imprints the P_s of ferroelectric layer in the pristine state, therefore the bilayer capacitor responses to an external small voltage excitation as a typical linear dielectric capacitor [10]. The total force exerted on the spontaneous dipole of the ferroelectric layer when an interface

trap charge is present can be expressed as follows under the assumption of mean-field approximation [10].

$$\text{Force} = \frac{\partial F_f}{\partial P_s} = 2\alpha P_s + 4\beta {P_s}^3 + 6\gamma {P_s}^5 - \left[{E_{ext}}^f + \frac{\sigma_i - P_s}{\varepsilon_0 \cdot l_f} \cdot \left(\frac{\varepsilon_b}{l_f} + \frac{\varepsilon_d}{l_d} \right)^{-1} \right]$$

The capacitance boosting during the NC operation can be explained in the view of internal field generation. When the external electric field is applied in the opposite direction to P_s, the reversed polarization cannot be electrostatically compensated, and the depolarization field is generated. Also, the internal field in the opposite direction to the depolarization field can be generated in the dielectric layer, however it has the identical direction with external voltage. Therefore, the electric field in the dielectric layer is amplified while the electric field in the ferroelectric layer decreases. The additional electric field across the dielectric layer can cause (transient) negative capacitance and capacitance boosting effects.

In the presence of an interface trap charge, the region where the polarization reversal appears is deviated from the V~0 region, so the operation voltage is increased. Accordingly, a large external field is added up to the internal field in the dielectric layer, a tunneling current can occur as shown in Figure 2.5 and Figure 2.6 [10]. The typical hysteresis observed in low-f P-V measurement of the ferroelectric/dielectric bilayer capacitors, which forms structurally dissimilar interfaces, can be explained as such tunnel-switch operation.

In the previous study, considering that the tunneling process of polarization bound charge through the dielectric layer is time-consuming process, the short time pulse-wise capacitance measurement was develoepd to observe negative capacitance effect with transient nature [11]. Using the measurement, the clear capacitance enhancement due to the transient negative capacitance effect of AO/BTO bilayer capacitor could be observed with wide voltage region as shown in Figure 2.7 [11]. However, the use of BTO material with perovskite crystal structure and their large film thickness was pointed out to limit the additional scale-down of the bilayer capacitor for the incorporation of current complementary metal-oxide semiconductor technology.

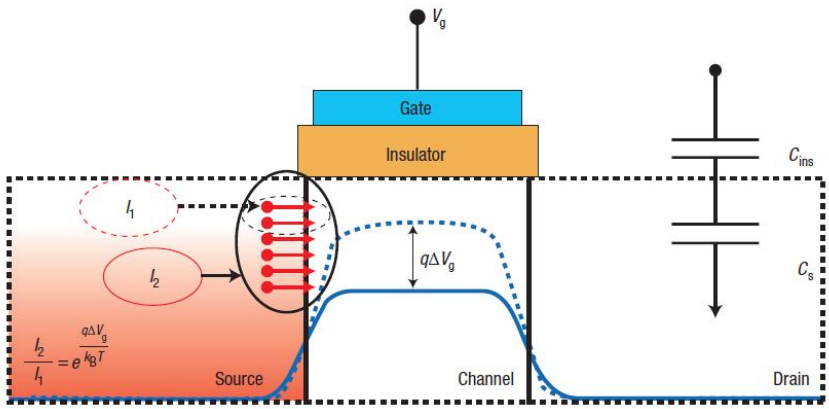

Figure 2.2 Schematic diagram of a field-effect transistor with the calculated channel current when the gate voltage is modulated [7].

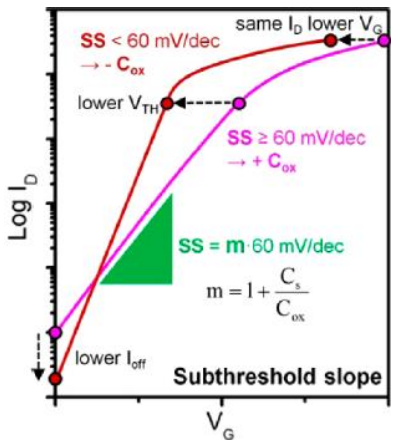

Figure 2.3 The expected change of subthreshold swing in the MOSFET when the negative capacitance effect is incorporated [8].

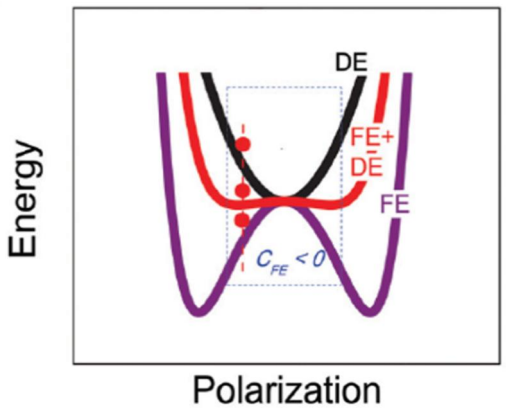

Figure 2.4 The calculated free energy diagram with a polarization change in a ferroelectric, a paraelectric, and their bilayer thin films [9].

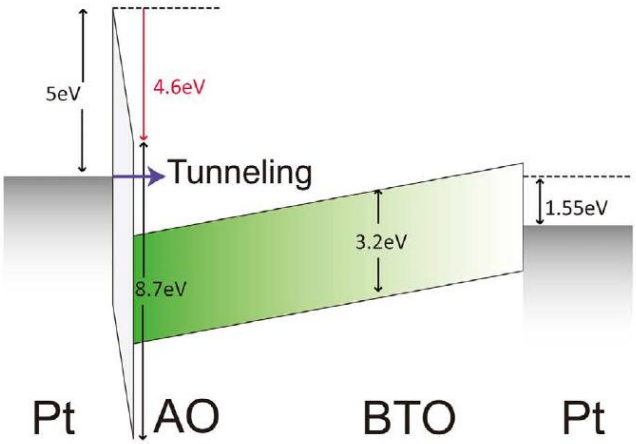

Figure 2.5 The band alignment of Pt/Al_2O_3/$BaTiO_3$/Pt capacitor and the expected tunneling current through the thin Al_2O_3 layer [10].

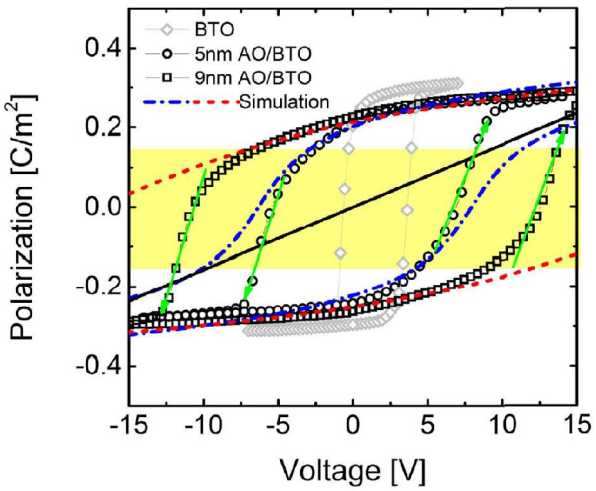

Figure 2.6 The hysteretic P-V curve observed in $BaTiO_3$ and $Al_2O_3/BaTiO_3$ bilayer capacitors, and the electrostatic simulation curves [10].

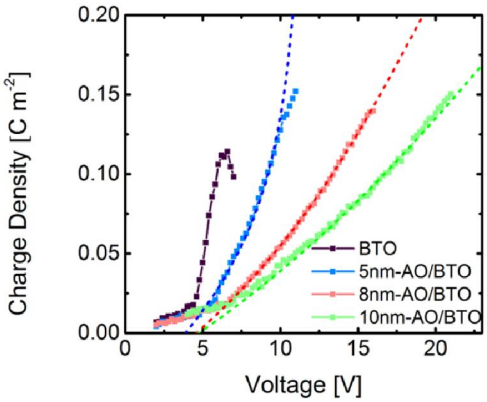

Figure 2.7 The discharge density according to the external voltage magnitude of $BaTiO_3$ and $Al_2O_3/BaTiO_3$ bilayer capacitors [11].

2.3. Bibliography

[1] K. Yao, S. Chen, M. Rahimabady, M. S. Mirshekarloo, S. Yu , F. E. H. Tay, T. Sritharan, L. Lu, *IEEE Trans. Ultrason. Ferr*., 58, 1968 (2011).

[2] L. C. Haspert, E. Gillette, S. B. Lee, G. W. Rubloff, *Energy Environ. Sci*., 6 , 2578 (2013).

[3] S. A. Sherrill, P. Banerjee, G. W. Rubloff, S. B. Lee, *Phys. Chem. Chem. Phys*., 13 , 20714 (2011).

[4] M. H. Park, H. J. Kim, Y. J. Kim, T. Moon, K. D. Kim, C. S. Hwang, *Adv. Energy Mater.*, 4, 1400610 (2014).

[5] F. Ali, X. Liu, D. Zhou, X. Yang, J. Xu, T. Schenk, J. Mueller, U. Schroeder, F. Cao, and X. Dong, *J. Appl. Phys.*, 122, 144105 (2017)

[6] S. Salahuddin, S. Datta, *Nano Lett*., 8, 405 (2008).

[7] V. V. Zhirnov and R. K. Cavin, *Nature Nanotechnology*, 3, 77 (2008).

[8] D. J. R. Appleby, N. K. Ponon, K. S. K. Kwa, B. Zou, P. K. Petrov, T. Wang, N. M. Alford, and A. O'Neill, *Nano Letter*, 14, 3864 (2014).

[9] A. I. Kahn, D. Bhowmik, P. Yu, S. J. Kim, X. Pan, R. Ramesh, and S. Salahuddin, *Appl. Phys. Lett.*, 99, 113501 (2011).

[10] Y. J. Kim, M. H. Park, Y. H. Lee, H. J. Kim, W. Jeon, T. Moon, K. D. Kim, D. S. Jeong, H. Yamada, C. S. Hwang, *Sci. Rep.*, 6, 19039 (2016).

[11] Y. J. Kim, H. W. Park, S. D. Hyun, H. J. Kim, K. D. Kim, Y. H. Lee, T. Moon, Y. B. Lee, M. H. Park, C. S. Hwang, *Nano Lett*. 17, 7796 (2017).

3. Scale-up and optimization of HfO_2-ZrO_2 solid solution thin films for the electrostatic supercapacitors

3.1. Introduction

Recently, ferroelectricity and field-induced ferroelectricity were found in doped or undoped HfO_2 [1-10], and in the HfO_2-ZrO_2 solid solution thin films [11-14]. The ferroelectricity of bulk HfO_2 and ZrO_2 was originally unexpected because their phase diagram shows only centrosymmetric crystal structures [15,16]. The ferroelectric phase of HfO_2 is now generally accepted as the metastable orthorhombic crystal structure with $Pca2_1$ space group (o-phase) [17,18], which has been reported to be stabilized only under the asymmetric high-pressure condition in ZrO_2 [19]. The reason why the metastable o-phase can be stabilized in HfO_2- or ZrO_2-based thin films is still under debate, and various factors, such as surface energy [20], film stress [14,21], doping [2], and TiN encapsulation [2,11], were suggested as affecting the polymorphism in HfO_2- or ZrO_2-based thin films [22]. The field-induced phase transition between the nonpolar tetragonal ($P4_2/nmc$; t-phase) and ferroelectric o-phase in doped HfO_2 and ZrO_2 was suggested as the origin for antiferroelectric-like double polarization-electric field (P-E) hysteresis [11,23]. It can be facilitated because the small energy difference between these two phases can be overcome by applying only 1-2 MV/cm of the electric field [23].

It was recently suggested that field-induced phase transition could be utilized for solid-state electrostatic energy storage [24]. Several papers reported the energy-storing behavior of the field-induced-ferroelectric (FFE) doped HfO_2 (and ZrO_2) thin

films [25-27]. Park et al. recently reported that a ~46 J cm^{-3} energy storage density (ESD) with 51% efficiency could be achieved in a ~9 nm-thick $Hf_{0.3}Zr_{0.7}O_2$ film [25]. Hoffmann et al. subsequently reported the energy storage properties of the ~9 nm-thick 5.6 mol% Si-doped HfO_2 film, where the thin film showed a ~40 J cm^{-3} ESD with a higher efficiency of ~80% due to its very slim P-E hysteresis [26]. Pešić et al. reported a ~37 J cm^{-3} ESD with ~51% efficiency in the FFE $ZrO_2/Al_2O_3/ZrO_2$ thin film capacitor, where the inserted Al_2O_3 layer was intended to work as a leakage current barrier [27]. Moreover, using the three-dimensional capacitor structure with a hole-patterned substrate, they achieved a ~930 J cm^{-3} ESD with ~70% efficiency when the device volume was taken as the projected area x the film thickness [27]. To date, the $Hf_{0.3}Zr_{0.7}O_2$ thin film showed the largest ESD value (~46 J cm^{-3}) among HfO_2- or ZrO_2-based films [25-27], which is comparable to the largest ESD value ever reported for perovskite structure based materials [28.29].

The large ESD value observed in the $Hf_{0.3}Zr_{0.7}O_2$ thin film, however, drastically decreased to ~32 and ~21 J cm^{-3} when the film thickness increased to ~12.4 and ~19.0 nm, respectively, which is considered a critical obstacle for the scale-up of the $Hf_{0.3}Zr_{0.7}O_2$ capacitors for storing an even larger quantity of energy in response to the high input voltage [25]. The significant decrease of the ESD with increasing film thickness seems to be due to the increase of the monoclinic phase (m-phase; $P2_1/c$) fraction in the HfO_2 thin films [12,25]. With increasing film thickness and the resulting decrease in the surface-to-volume ratio, the polymorphism in $Hf_{1-x}Zr_xO_2$ thin films is largely governed by the bulk free energy and not by the surface energy, which leads to the formation of m-phase. It was suggested that the reversible phase

transition between the m- and o-phases is hardly possible [30], and as such, the FFE properties might be improbable within films dominated by the presence of the m-phase.

The formation of the m-phase is believed to result from the crystallization during the atomic layer deposition (ALD) process without a TiN capping layer [2,11,30]. It was suggested that the TiN encapsulation could suppress the formation of the m-phase by prohibiting the surface diffusion or by suppressing the shear strain for m-phase formation [22]. These factors suggest that crystallization during ALD needs to be prevented to deter m-phase formation. As the film grown by ALD generally shows a very low growth rate (~0.1 nm cycle^{-1}) with one cycle of several tens of seconds, growing a 10 nm-thick film usually takes ~20 min, which is long enough to induce in-situ (partial) crystallization if the ALD temperature is relatively high (>250 ^{o}C). Also, there have been requirements for the lower temperature deposition of (anti-) ferroelectric materials for the use of the transparent or flexible substrates, and in this regard, several papers reported on the attempts to reduce the thermal budget necessary for the preparation of ferroelectric HfO_2 thin film [31-34]. Especially, since the HfO_2-ZrO_2 solid solution has a lower crystallization temperature than other doped-HfO_2, the importance of low ALD temperature is expected to be greater. In this study, therefore, the ALD temperature (T_{dep}) of the $Hf_{0.5}Zr_{0.5}O_2$ thin film was varied from 180 to 280 ^{o}C, and the structural variation and the accompanying energy storage behavior of the thin films with a wide thickness range (6 - 40 nm) were systematically studied. The $Hf_{0.5}Zr_{0.5}O_2$ thin films deposited at a low temperature (210 ^{o}C) showed a high ESD of 35 J cm^{-3} even up to 40 nm thickness. With the optimized condition,

the largest ESD of ~55 J cm^{-3} with ~57% efficiency could be achieved. Moreover, such large ESD was maintained up to 175 ºC without significant degradation, and excellent switching endurance was confirmed up to 10^{10} bipolar switching cycles.

3.2. Experimental

$Hf_{0.5}Zr_{0.5}O_2$ thin films were deposited via a thermal atomic layer deposition (ALD) process on a TiN bottom electrode at various T_{dep}'s. $Hf[N(C_2H_5)CH_3]_4$ (TEMA-Hf), $Zr[N(C_2H_5)CH_3]_4$ (TEMA-Zr), and ozone with 180 g m^{-3} concentrations were used as a Hf precursor, a Zr precursor, and an oxygen source, respectively. The Ar gas with the flow rate of 200 standard cubic centimeter per min (sccm) were used as a carrier and purge gas in the cross-flow type ALD chamber, and the mixture of O_2 (1350 sccm) and N_2 (10 sccm) gas were used for the ozone generation. A 50 nm-thick TiN bottom electrode was prepared via DC reactive sputtering with 5 kW DC power, Ar 15 sccm / N_2 85 sccm gas flow, and at the 200°C temperature of processing on a Ti (5 nm)/SiO_2 (100 nm)/Si substrate. The TiN top electrodes were also prepared via similar DC reactive sputtering with 100 W DC power, Ar 20 sccm / N_2 1 sccm gas flow, and at the 110°C temperature of processing. The $Hf_{0.5}Zr_{0.5}O_2$ thin films were deposited at a 1:1 (HfO_2:ZrO_2) ALD cycle ratio, and X-ray fluorescence (XRF, ThermoScientific, ARL Quant'X) confirmed the 1:1 (Hf:Zr) atomic ratio of the thin films regardless of the T_{dep}, which is probably due to the similar chemical properties of the TEMA-Hf and TEMA-Zr precursors. The growth rate of the $Hf_{0.5}Zr_{0.5}O_2$ thin film slightly increased from ~0.12 nm/cycle at 280 °C to ~0.13 nm/cycle at 180 °C. To characterize the electrical properties, a Pt (30 nm)/TiN (5 nm) top electrode was fabricated via DC (reactive) sputtering using a shadow mask with a 300-□m-diameter dot pattern (TiN contacts the $Hf_{0.5}Zr_{0.5}O_2$ film). After depositing the top electrode, post-metallization

annealing was performed by rapid thermal annealing at 600 ºC for 20 s in an N_2 atmosphere to crystallize the $Hf_{0.5}Zr_{0.5}O_2$ thin films.

The polarization - electric field (P-E) and capacitance - electric field (C-E) curves were measured using a ferroelectric tester (Aixacct Systems, TF Analyzer 2000) with a 1 kHz measurement frequency and an impedance analyzer (HP4194A, Hewlett Packard) with a 50 mV AC field and 10 kHz AC field frequency, respectively. The C-E curves were converted to dielectric constant – electric field ($\square_r$-E) curves using the film thickness and electrode area. The current density-electric field curves were measured using a semiconductor parameter analyzer (HP 4140B, Hewlett Packard). The top electrode was used to bias the capacitor while the bottom electrode was grounded during the measurements. The film thickness and density were measured via X-ray reflectance (XRR, PANalytical, X'Pert Pro) and XRF. For the crystal structure analysis, an X-ray diffractometer (XRD, PANalytical, X'Pert Pro) was used with a glancing angle incidence X-ray diffraction (incidence angle = 0.5º) geometry after ~5 nm-thick TiN films were deposited on the whole surface area of the $Hf_{0.5}Zr_{0.5}O_2$ thin film. For the morphological analysis, a scanning electron microscope (S-4800, Hitachi) was used.

3.3. Results and Discussions

3.3.1. Field-induced Ferroelectric $Hf_{0.5}Zr_{0.5}O_2$ Thin Films

The chemical, physical, and structural properties of the $Hf_{0.5}Zr_{0.5}O_2$ thin films deposited at various T_{dep}'s were examined first. Figure 3.1a shows the X-ray reflectance (XRR) spectra of the ~10 nm-thick $Hf_{0.5}Zr_{0.5}O_2$ films deposited at various T_{dep}'s, and the mass densities and growth rates (film thickness divided by the number of ALD cycles) from the fitting of the XRR data are plotted in Figure 3.1b as a function of T_{dep}. The fitting of the XRR spectra was performed under the assumption of homogeneous layers comprising a stack of the $Hf_{0.5}Zr_{0.5}O_2$ layer and the underlying TiN electrode. The TiN electrode on a $Ti/SiO_2/Si$ substrate was separately measured again to reconfirm the mass density and the thicknesses of the layers underneath the $Hf_{0.5}Zr_{0.5}O_2$ film. The mass density of the $Hf_{0.5}Zr_{0.5}O_2$ thin film increased from ~5.8 g cm^{-3} at 180 ºC to ~6.7 g cm^{-3} at 280 ºC. A similar mass density increase was reported in the authors' previous study on HfO_2 deposited using the identical TEMA-Hf and ozone as a Hf precursor and an oxygen source, respectively. In that report, the mass density of the thin film increased from ~7.0 to ~8.1 g cm^{-3} as the T_{dep} increased from 200 to 280 ºC [10]. Growth rate of the $Hf_{0.5}Zr_{0.5}O_2$ thin film, on the other hand, slightly decreased from ~0.13 nm $cycle^{-1}$ at 180 ºC to ~0.12 nm $cycle^{-1}$ at 280 ºC [10]. These variations in the deposition behavior are believed to be due to the certain incorporation of low-density components into the thin film at the lower T_{dep}.

Figure 3.1c shows the variation of the C atomic concentration from the Auger electron spectroscopy of the $Hf_{0.5}Zr_{0.5}O_2$ thin film deposited at 180 - 280 ºC. The C

concentration of the $Hf_{0.5}Zr_{0.5}O_2$ thin film was estimated by averaging the relative C atomic concentration within the $Hf_{0.5}Zr_{0.5}O_2$ film region during the AES depth profiling (see Figure 3.2) to avoid undesirable sources of impurities at the surface and interface regions. The C concentration clearly showed a decreasing tendency from ~8 to ~3 at% as the T_{dep} increased from 180 to 280 °C. It is noted that there is a slight increase in the growth rate and C concentration at 280 °C compared with those at 260 °C. This is possibly due to the partial involvement of chemical vapor deposition-like reaction during the deposition of HZO thin film at this high temperature. For the case of the N impurities, their concentrations could not be quantitatively analyzed possibly due to their low concentration, below the sensing limit of AES. In addition, due to the extremely small thicknesses of the $Hf_{0.5}Zr_{0.5}O_2$ films, the detection of an N signal in the $Hf_{0.5}Zr_{0.5}O_2$ films could be interfered with by that from the TiN bottom electrode. This difficulty does not necessarily mean, however, that N impurities do not exist in $Hf_{0.5}Zr_{0.5}O_2$ films, or that the N impurities will not influence the polymorphism of $Hf_{0.5}Zr_{0.5}O_2$ films. According to the previous reports on the chemical reactions during the ALD of HfO_2 thin films using a TEMA-Hf precursor, the residual byproducts were expected to have a certain amount of N impurities [10,35,36]. Kim et al. could experimentally identify the increase of N in the HfO_2 thin films at the extremely low deposition temperature (<100 °C) [35]. Also, a slight evolution of N 1s peak at the decreased T_{dep} down to 200 °C could be observed in the X-ray photoemission spectroscopy from the authors' previous study on HfO_2 thin film (see Figure 3.3) [10]. Liu et al. explained the origin of the increasing residual impurities at a low T_{dep} when a HfO_2 thin film was deposited using O_3 [36]. They

found that due to the formation of an unstable $N[CH_3]C_2H_5$ intermediate byproduct, proton transfer could occur from a certain portion of the TEMA-ligand to the intermediate byproduct [36]. If such chemical reaction occurred, the proton-deficient TEMA-ligand would have a higher binding energy with the surface even after the ligand exchange reaction [36]. Therefore, more C/N elements could be found in the HfO_2 layer at a lower T_{dep}, where the thermal energy for the desorption decreased. According to their model, the expected N concentrations in the $Hf_{0.5}Zr_{0.5}O_2$ films deposited at 180 and 280 °C were ~3 and ~1 at%, respectively. Therefore, N atoms were considered present, along with C impurities, in the $Hf_{0.5}Zr_{0.5}O_2$ films in this study.

The residual C/N impurities were reported to stabilize the high-symmetry metastable phases in HfO_2 [9,37,38]. Jung et al. calculated that the C dopant in the HfO_2 matrix could decrease the bulk free energy of the t-phase compared to that of the m-phase, especially when the C atoms are coupled with charged oxygen vacancies [37]. Cho et al. also reported that the t-phase could be stabilized with increasing C impurities by decreasing the power for ozone generation for their thermal ALD system [38]. Furthermore, Xu et al. reported the stabilization of the ferroelectric o-phase when the HfO_2 thin film was doped with N, whose concentration was even lower than 1% [9]. In the report, an N doping concentration of only 0.34% was enough to induce switchable polarization ($P_r^+ - P_r^-$) of ~21 □C cm^{-2} [9]. These studies suggest that the crystal structure of the $Hf_{0.5}Zr_{0.5}O_2$ thin film can be affected by the change of T_{dep} through the change in residual C/N impurities.

It was reported that the increase in the C concentration in the HfO_2 thin film could decrease the average grain size (D_{ave}) of the HfO_2 thin films [38]. Thus, in this study, the grain size distributions of the $Hf_{0.5}Zr_{0.5}O_2$ thin films deposited at various T_{dep}'s were analyzed using a watershed method implemented by the Gwyddion software [39]. The films grown at different T_{dep}'s were post-deposition annealed at 600 ºC for 20 sec under an N_2 atmosphere, using a rapid thermal annealing system. As in the previous studies on HfO_2 [10], a small difference in the D_{ave} was induced as the T_{dep} changed, shown as scanning electron microscopy (SEM) images in Figure 3.1d. The plan-view SEM images used for grain size analysis are shown in Figure 3.4 while the grain size distributions of the $Hf_{0.5}Zr_{0.5}O_2$ films deposited at various T_{dep}'s are shown in Figure 3.5a. The D_{ave}'s of the $Hf_{0.5}Zr_{0.5}O_2$ thin films deposited at 200, 220, 240, 260, and 280 ºC were 5.8, 6.4, 6.6, 6.7, and 6.7 nm, respectively. The film grown at 180 ºC did not show an obvious grain structure in SEM, and as such, it was excluded in the dataset. Such grain size variation, however, was insufficient to significantly change the relative fractions of the stable phases in the $Hf_{0.5}Zr_{0.5}O_2$ thin films. The expected relative fractions of the m-, o-, and t-phases are shown in Figure 3.5b, which were calculated based on the surface energy model suggested by Materlik and coworkers [20]. According to the model, the expected volumetric fraction of the t-phase ranges from ~12 to ~21%, while that of the o-phase ranges from 88 to 79%. Therefore, the polymorphism in $Hf_{0.5}Zr_{0.5}O_2$ thin films might be affected by the grain size variation as well as the C/N impurities with varying T_{dep}. For low-T_{dep} HfO_2 films, it was also suggested that the formation of the o-phase could not be understood solely

from the grain size effect and that C doping might also affect the stabilization of the metastable phases [10].

Figure 3.6 shows the grazing incidence X-ray diffraction (GIXRD) results within the 20 - 50° 2θ range of the TiN (5 nm)/$Hf_{0.5}Zr_{0.5}O_2$ (9 nm)/TiN (50 nm) structure after post-metallization annealing (PMA) at 600 °C for 20 sec under an N_2 atmosphere using a rapid-thermal-annealing system. In the previous study on HfO_2, the m-phase was destabilized by the o-phase dominance, which had been identified from the decrease in the intensities of the diffraction peaks at around 2θ = 28.5° and 31.6° (m(-111) and m(111), respectively), with decreasing T_{dep} after the identical PMA process [10]. In this study, however, the m-phase of HfO_2 was already destabilized at T_{dep} = 280 °C by forcing a solid solution with ZrO_2, and as such, m-phase peaks were not observed, as shown in Figure 3.6. Instead, the peak from the t- or o-phase at around 2θ = ~30.5° appeared in the whole T_{dep} range. Figure 3.6b shows the GIXRD patterns within the narrower 2θ range from 27 to 33° analyzed with a longer acquisition time per step to achieve a higher signal-to-noise ratio. Here, the peak at around ~30.5° shifted towards a higher 2θ direction as the T_{dep} decreased. This phenomenon can be ascribed to the change of the dominant phase within the $Hf_{0.5}Zr_{0.5}O_2$ thin film from the o-phase (2θ = ~30.4° of o(111)) for a high T_{dep} to the t-phase (2θ = ~30.8° of t(011)) for a low T_{dep}. A similar trend was reported for $Hf_{0.5}Zr_{0.5}O_2$ films in a previous study [12].

From the chemical, physical, and structural properties from Figure 3.1 to 3.6, the electric properties of $Hf_{0.5}Zr_{0.5}O_2$ films are also believed to be strongly affected by

T_{dep}. The transition between the o- and t-phases in $Hf_{1-x}Zr_xO_2$ thin films can be understood based on the first-order phase transition theory [40-43]. Figure 3.7a-c and d-f show the schematic energy-polarization (F-P) and polarization-electric field (P-E) diagrams based on the Landau-Ginzburg-Devonshire (LGD) model [41]. Equation (3.1) shows the relation between the F and P of the $Hf_{0.5}Zr_{0.5}O_2$ thin film, whereas equation (3.2) shows that between E and P based on the LGD model [41].

$$F = \frac{1}{2}\alpha_0\{T - T_0(x, t, r, T_{dep})\}P^2 + \frac{1}{4}\beta P^4 + \frac{1}{6}\gamma P^6 - P \cdot E \quad (3.1)$$

$$E = \alpha_0\{T - T_0(x, t, r, T_{dep})\}P + \beta P^3 + \gamma P^5 \quad (3.2)$$

Here, α_0, β, and γ are the Landau coefficients, and x, t, r, and E are the Zr content, film thickness, grain radius, and external electric field, respectively. T_0 is the Curie-Weiss temperature, where the shape of the F-P curve changes between the double- and triple-potential well shapes, which is determined by the Zr content, film thickness, and grain radius. These parameters are determined by the ALD conditions, including the T_{dep}, which makes the parameters process-dependent. T_0 may also be affected by several other factors, but only the factors mentioned above, which are believed to be the most critical, were considered in this study for convenience's sake.

In Figure 3.7, three characteristic temperatures (T_C, T_1, and T_2) other than T_0 can be noted. T_C is the Curie temperature at which the free energy of the polar and nonpolar phases become equivalent. Below T_C, the stable phase at zero electric field is a polar phase, as can be seen in Figure 3.7a, while above T_C, the stable phase is a

nonpolar phase, as can be seen in Figure 3.7b. As a result, a characteristic single-hysteresis can be observed below T_C (Figure 3.7d), whereas a so-called "broken" hysteresis can be observed between T_C and T_1 (Figure 3.7e). T_1 is the higher limit to show ferroelectricity, above which the polar phase is no more metastable at zero electric field, as can be seen in Figure 3.7c. Above T_1, double hysteresis can be observed, as can be seen in Figure 3.7f, but this double hysteresis with field-induced phase transition disappears above the critical temperature of field-induced ferroelectricity, T_2. A more detailed explanation of this can be obtained from the previous studies [20,42,44].

In the previous studies, the effects of the Zr content and film thickness on the polymorphism and the resulting electric properties were examined. Mueller et al. reported the change of the P-E curve of $Hf_{1-x}Zr_xO_2$ films with various Zr contents [11]. In that report, the shape of the P-E curves changed from a linear dielectric-like one (pure HfO_2) to single ferroelectric hysteresis ($Hf_{0.5}Zr_{0.5}O_2$) to FFE double hysteresis (pure ZrO_2) at the film thickness of 9 nm, implying a decrease of T_0 with increasing Zr content from 0.5 to 1.0 [11]. Park et al. examined the temperature-dependent P-E characteristics of $Hf_{1-x}Zr_xO_2$ films with various Zr contents (x = 0.7 – 0.9) [45], and suggested that the T_0 of the $Hf_{1-x}Zr_xO_2$ thin film decreases with increasing x, which was consistent with what Mueller et al. previously reported [11]. A similar trend was also confirmed in Si-doped HfO_2 thin films by Hoffmann and co-workers [26]. The film thickness is another factor that alters the T_0 of $Hf_{1-x}Zr_xO_2$. Park et al. examined the change of the P-E curves of $Hf_{0.5}Zr_{0.5}O_2$ films thinner than 8 nm, and reported the transition from the o- to the t-phase with decreasing film thickness, implying that the

T_0 also decreases with decreasing film thickness [46]. Similar results on $Hf_{0.5}Zr_{0.5}O_2$ and $Hf_{0.3}Zr_{0.7}O_2$ films thicker than 10 nm were found in other studies, but the polymorphism in thicker films could not be explained solely by the LGD model due to the involvement of the m-phase [12,25]. The Zr concentration and the film thickness (and the accompanying grain size) are the material parameters, and as such, it is somehow natural to see the property modulation with variations in these parameters. In thin-film processing, however, the process parameters, most notably the T_{dep}, would render critical influences on these material parameters, affecting the value of T_0.

Figure 3.8a-e show the P-E curves of $Hf_{0.5}Zr_{0.5}O_2$ films deposited at various temperatures (from 280 to 200 ^oC), and Figure 3.4f-j show the corresponding ε_r-E curves. From this point, the film grown at a higher T_{dep} (280 ^oC) was taken as a reference and is thus described first, and the films grown at a lower T_{dep} are subsequently described to elucidate the T_{dep}'s effects. The current density-electric field (J-E) curves of these samples are shown in Figure 3.9. Also, the dielectric loss-electric field curves corresponding to the Figure 3.8f-j are shown in Figure 3.10, which showed typical (anti-) ferroelectric insulating capacitors' of which curves show a low value and evolution of peaks related to the polarization change. Except the 10 nm-thick $Hf_{0.5}Zr_{0.5}O_2$ film deposited at 200 ^oC, the dielectric losses are lower than 0.06, suggesting that the leakage current through the $Hf_{0.5}Zr_{0.5}O_2$ films are effectively suppressed. The maximum dielectric loss of 200 ^oC deposited film is also lower than 0.11. It should be noted that the experimental P-E curves are different from the theoretical P-E curves in Figure 3.7a-c due to the spatial distribution of T_0, which

could be incurred by the grain size and orientation distributions in polycrystalline $Hf_{0.5}Zr_{0.5}O_2$ thin films [20,26]. At the highest T_{dep} (280 °C) the crystal structure of the $Hf_{0.5}Zr_{0.5}O_2$ thin film is supposed to be mainly ferroelectric o-phase; therefore, the F-P curve should have two global minimums, as shown in Figure 3.7a. The shallow local minimum state located in P=0 of the F-P diagram reflects a potential well for the nonpolar t-phase [47], but the existence of the intermediate t-phase cannot be externally observed in the P-E hysteresis curve, as can be seen in Figure 3.7a, because the polarization switching should be mediated by reverse domain nucleation and growth. The local potential well at P=0 affects only the kinetic energy barrier between the two P_r states and the resulting coercive field [43,48]. The P-E (Figure 3.4a) and ε_r-E (Figure 3.8f) characteristics of the $Hf_{0.5}Zr_{0.5}O_2$ thin films deposited at 280 °C were similar to those of the $Hf_{0.5}Zr_{0.5}O_2$ thin films deposited with similar conditions in the previous studies [13]. With decreasing T_{dep}, however, the P-E diagram appears to show a broken hysteresis loop, which suggests that the free energy difference between the t- and o-phases gradually decreases and that at a certain T_{dep}, the free energy of the t-phase becomes lower than that of the o-phase [42,44]. The broken hysteresis can be characterized by P-E hysteresis with intermediate plateau regions between the two P_r states, as can be seen in Figure 3.7e. Such electric behavior can be seen from the experimental P-E curves of the $Hf_{0.5}Zr_{0.5}O_2$ film deposited at 220 °C in Figure 3.8d. Due to the polycrystalline nature of the $Hf_{0.5}Zr_{0.5}O_2$ films, however, the change of the P-E curve near T_C cannot be discontinuous, as theoretically expected for the first-order phase transition [20,26]. When the T_{dep} was further decreased to 200 °C, the P-E loop became further distorted and finally showed an

FFT, which could be incurred by the phase transition from the t- to the o-phase at a sufficiently high field, as shown in Figure 3.8e. This observation means that the structural change occurring during the PMA at a sufficiently low T_{dep} mostly destabilized the o-phase and stabilized the t-phase instead. This FFE response was shown in the P-E (Figure 3.8e) and ε_r-E response (Figure 3.8j) of the $Hf_{0.5}Zr_{0.5}O_2$ thin film deposited at 200 ºC.

3.3.2. Scale-up of HfO_2-ZrO_2 Solid Solution Thin Films

Figure 3.11a shows the schematic diagram that illustrates an energy storage behavior of FFE materials in the P-E diagram. In the Figure 3.11a, only the first quadrant of the P-E diagram is presented for simplicity. As indicated in the first formula of Figure 3.11a, the change of the stored energy is presented as the electrical work done during the application and removal of the electric field on the electrostatic capacitor. The red area represents the ESD, which refers to the electrostatic energy density that can be restored when the electric field is removed. The green area, enclosed in the P-E hysteresis, is the energy loss dissipated during the hysteretic motion of polarization with the varying electric field. The above two components constitute the total energy consumption during the initial application of an electric field on the FFE capacitor. The efficiency can then be calculated as a ratio of the ESD to the total energy consumption (ESD + Loss) as indicated in Figure 3.11a. Figure 3.11b shows the ESD changes according to the thickness of the $Hf_{0.3}Zr_{0.7}O_2$ thin films deposited at 280 ºC, reproduced from Ref. 25 (black square symbol) and the $Hf_{0.5}Zr_{0.5}O_2$ thin films deposited at 210 ºC (red circle symbol). The $Hf_{0.3}Zr_{0.7}O_2$ thin

film shows a drastic decrease of the ESD from ~46 to ~21 J cm^{-3} when the film thickness increased from ~9.2 to ~19.0 nm, and a slightly increased value to ~24 J cm^{-3} at the ~29.0 nm again owing to the small increase of the maximum applicable electric field [25]. For the case of the $Hf_{0.5}Zr_{0.5}O_2$ films deposited at 210 ºC, however, no distinctive degradation of the P-E curve was found when the film thickness increased from ~10.0 to ~20.2 nm. At above ~20.2 nm, the P_{max} started slightly declining, and thus, the ESD showed a gradual decrease. Nonetheless, the ESD can be as high as ~34 J cm^{-3} even up to the thickness of 40 nm. The corresponding P-E curves of the $Hf_{0.5}Zr_{0.5}O_2$ films are shown in Figure 3.12a. Figure 3.12b and c show the ε_r-E and J-E characteristics with the corresponding films. Figure 3.13 shows the dielectric loss-electric field curves corresponding to the Figure 3.12b. Figure 3.11c shows the corresponding efficiency changes on the film thickness. The $Hf_{0.3}Zr_{0.7}O_2$ thin film deposited at 280 ºC showed ~40 - 50% efficiency (black square symbol) while the $Hf_{0.5}Zr_{0.5}O_2$ thin film deposited at 210 ºC showed a much higher value of ~62% (red circle symbol). On the efficiency tendency of the $Hf_{0.3}Zr_{0.7}O_2$ thin film, the drastic decrease is noted when the thickness increase from ~9.2 nm to ~12.4 nm, which is mostly ascribed to the decrease in the critical field for the phase transition as well as the increase of internal area of the P-E hysteresis. The increased efficiency of $Hf_{0.5}Zr_{0.5}O_2$ thin film compared to the $Hf_{0.3}Zr_{0.7}O_2$ thin film is believed to have resulted from the decrease in the electric loss, which might have been strongly related to the kinetics of the field-induced phase transition. The effect of the T_{dep} on the phase transition kinetics, however, cannot be elucidated in this study. It is possible that the C and N impurities facilitate the nucleation of the phases by serving as the preferred

sites for heterogeneous nucleation. Further studies are required to investigate the kinetics of field-induced phase transition in $Hf_{1-x}Zr_xO_2$ films.

As stated in the Introduction section, the different thickness dependency of the ESD seems to be associated with the degree of crystallization of the as-deposited state. Figure 3.11d shows the relative crystallinity compared to the films after the PMA process, which was calculated based on the GIXRD patterns shown in Figure 3.14. The crystallinity of the as-deposited state was estimated using the peak area within the 2θ range of 27 - 33°, where the o(111)/t(011) peak at ~30.5°, the m(-111) peak at ~28.5°, and the m(111) peak at ~31.5° exist. To estimate the crystallinity of the as-deposited films, the annealed samples were assumed to be fully crystallized, and the total area of the diffraction peaks in the GIXRD patterns of the as-deposited films was divided by such after the PMA process. For the $Hf_{0.3}Zr_{0.7}O_2$ thin film deposited at 280 °C, it was already crystallized by ~90% at the ~20 nm thickness in the as-deposited state (black square symbol) and was completely crystallized at the ~30 nm thickness. For the $Hf_{0.5}Zr_{0.5}O_2$ thin film deposited at 210 °C, on the other hand, it was crystallized by less than ~10% at the ~20 nm thickness, and was crystallized by only ~31% even at the ~40 nm thickness (red-circle symbol). Haussmann et al. examined the crystallization during the ALD process for HfO_2 and ZrO_2 [50]. In their report, they revealed that the crystallization of HfO_2 and ZrO_2 during the ALD process is a thermally activated process, and that the kinetic energy barrier for the nucleation process for HfO_2 and ZrO_2 are 38 and 24 kJ mol^{-1}, respectively [50]. Therefore, the crystallinity of the as-deposited $Hf_{0.5}Zr_{0.5}O_2$ films should decrease with decreasing T_{dep} and Zr content. The relatively lower crystallinity of the $Hf_{0.5}Zr_{0.5}O_2$ film

deposited at 210 ºC compared to that of the $Hf_{0.3}Zr_{0.7}O_2$ film deposited at 280 ºC can be understood based on the above two factors. As a result, the much higher fraction of the $Hf_{0.5}Zr_{0.5}O_2$ film can be crystallized with TiN encapsulation during the PMA process, resulting in a lower m-phase fraction [2,11].

3.3.3. Optimization and Reliability

The optimization of the $Hf_{0.5}Zr_{0.5}O_2$ thin films to find the largest ESD condition were carried out by systematically controlling the two variables for T_0, the thickness and T_{dep}, while the Zr content was kept constant for the convenience of experiment. The effect of Zr content on the ESD was previously examined on the $Hf_{1-x}Zr_xO_2$ thin films deposited at 280 ºC, where the Zr content of x = 0.7 exhibited the largest ESD [25]. In this experiment, however, the increase of Zr content more than x = 0.5 can significantly decrease T_0 of the thin film when it is combined with other variables for T_0, suppressing the FFE response. Therefore, the Zr content was set as x = 0.5. The P-E curves and the corresponding energy storage properties of the $Hf_{0.5}Zr_{0.5}O_2$ thin films deposited at several different T_{dep}'s (215, 230, 245, 260, and 280 ºC) are shown in Figure 3.15 and 3.16, respectively. Specifically, Figure 3.17a and b show the P-E curves and the corresponding energy storage properties of the ~5.8 to ~10.2 nm $Hf_{0.5}Zr_{0.5}O_2$ thin films deposited at 215 ºC at their maximum electric field, respectively. With decreasing film thickness, the slight increase of the critical field for the transition from the t-phase to the o-phase can be observed, which is due to the stabilization tendency of the nonpolar t-phase compared to the o-phase by the surface energy effect as the thickness decreases [46]. This also indicates the decrease of T_0 at

a smaller thickness. Among the thin films with various thicknesses and deposited at different T_{dep}'s, it was found that the ~7.1 nm-thick $Hf_{0.5}Zr_{0.5}O_2$ film deposited at 215 ^oC exhibited the largest ESD (~55 J cm^{-3}) and ~57% efficiency. The ESD found in this film is larger than the previously reported ESD for the ~9 nm-thick $Hf_{0.3}Zr_{0.7}O_2$ film by ~9 J cm^{-3}, and it also showed the improved thermal and switching endurance (shown below). The larger ESD compared with that of the previously reported $Hf_{0.3}Zr_{0.7}O_2$ thin film is attributed to the increase of efficiency and the maximum allowable electric field (E_{max}). The E_{max} increased by ~0.44 MV cm^{-1} compared with that of the $Hf_{0.3}Zr_{0.7}O_2$ thin film, and it is also slightly larger than those of the thicker films deposited at the same T_{dep} (215 ^oC), as shown in Figure 3.6a. It cannot be clearly understood at the moment why the E_{max} increased with decreasing film thickness down to 7.1 nm. At a low T_{dep}, also, more C and N impurities exist in $Hf_{0.5}Zr_{0.5}O_2$ films, implying a higher leakage current level at the low electric field region (Figure 3.9). According to the several literatures, the following three factors can be suggested as the possible causes of the E_{max} increase with decreasing film thickness down to ~7 nm. First, it was reported that oxygen vacancy diffusion could be suppressed when the $Hf_{0.5}Zr_{0.5}O_2$ thin film is deposited at a low temperature because the activation energy for the movement of the oxygen atom could increase due to the C/N-V_O (oxygen vacancy) complex formation [37,51]. Second, the interface quality improvement can also potentially contribute to the suppression of the breakdown when the $Hf_{0.5}Zr_{0.5}O_2$ thin film is deposited at a low temperature [52,53]. The thermally activated diffusion between the TiN electrode and the $Hf_{0.5}Zr_{0.5}O_2$ films may be suppressed at a low T_{dep}. Third, the breakdown field of the HfO_2 thin film is

known to increase with the decrease of the film thickness due to the change in the maximum kinetic energy of the charge carriers within the thin film [54]. The maximum kinetic energy, which is closely related to the bond breakage rate, generally decreases as the film thickness decreases because the charge carriers are given a smaller accelerating distance [55]. At an excessively thin film (here, <~7 nm), however, the degraded electrical performance of the interface portion damaged by the adverse chemical interaction dominates, which leads to E_{max} decrease. Therefore, there must be an optimal thickness for the largest E_{max}, which was ~7.1 nm in the case of the $Hf_{0.5}Zr_{0.5}O_2$ thin film in this study. Therefore, the results of a further examination of the electrical performances of such optimal film are shown in Figure 3.18.

Figure 3.18 shows the reliability characteristics of the ~7.1 nm-thick $Hf_{0.5}Zr_{0.5}O_2$ film deposited at 215 ºC. Figure 3.18a shows the change of the P-E curves during the field cycling with a pulse field amplitude of ~4.23 MV cm^{-1} at the cycling frequency of 500 kHz. Figure 3.18b shows the corresponding ESD and efficiency change up to 10^{10} switching cycles. With the increase in the field cycling number, the ESD slightly decreased from ~46 J cm^{-3} at the pristine state to ~42 J cm^{-3} after 10^{10}-time switching. This might be due to the increase of the P_r during the field cycling, originating from the permanent phase transition from the t- to the o-phase. This is well known as the "wake-up effect" which is a commonly observed phenomenon when repeated electric-field cycling is applied on a doped HfO_2 thin film [56]. The efficiency remained almost constant at ~62% when averaged between the positive and negative electric field regions. This might be due to the decrease of the critical field for the

phase transition from the t- to the o-phase, which might have alleviated the possible increase of the internal area in the P-E hysteresis by the P_r increase. Figure 3.18c shows the P-E curve changes at various temperatures (from 25 to 175 ºC); the P-E curve at 25 ºC was obtained again after the high-temperature measurements. A gradual increase of the critical field for the phase transition could be observed as the temperature increased, especially on the negative side of the P-E curves. This result is in accordance with the previous study of Park et al., where they also reported an increase of the critical field in the FFE $Hf_{0.3}Zr_{0.7}O_2$ thin film as the temperature increased from 25 to 175 ºC [25,45]. Moreover, Müller et al. reported a decrease of the critical field and an increase of the P_r in the $Hf_{0.3}Zr_{0.7}O_2$ thin film as the temperature decreased from -43 to -197 ºC [11]. Materlik et al. mentioned that in the HfO_2-ZrO_2 solid solution, the t-phase becomes favorable compared to the o-phase at a high temperature owing to its higher crystal symmetry compared to that of the o-phase [20]. In other words, the electric field needed for phase transition from the t- to the o-phase becomes high due to the increased free energy difference between the o- and the t-phase as the temperature increases [20]. Nevertheless, the change of the P-E curve was negligible; therefore, the ESD and efficiency characteristics of the ~7.1 nm-thick $Hf_{0.5}Zr_{0.5}O_2$ film deposited at 215 ºC maintained a large value up to 175 ºC, as shown in Figure 3.18d, which demonstrates the possible compatibility of this material with high-temperature operation.

3.4. Summary

In summary, the polymorphism and resulting energy storage behavior of atomic-layer-deposited $Hf_{0.5}Zr_{0.5}O_2$ thin films were systematically studied by controlling the deposition temperature and the film thickness. The dominant crystalline phase in the $Hf_{0.5}Zr_{0.5}O_2$ thin film gradually transformed from the ferroelectric o-phase to the FFE t-phase when the deposition temperature decreased from 280 to 200 °C. Such behavior can be understood from the doping effect of C and N from the ligands of the TEMA-Hf and TEMA-Zr precursors into the thin film in combination with the slight decrease in grain size. The energy storage densities of the $Hf_{0.5}Zr_{0.5}O_2$ thin films were compared with those of the previously reported FFE $Hf_{0.3}Zr_{0.7}O_2$ thin films with a wide thickness range. Even with the increased thickness up to 40 nm, the energy-storing properties of the $Hf_{0.5}Zr_{0.5}O_2$ thin film deposited at 210 °C were less degraded due to the minimal formation of an undesirable monoclinic phase compared to the $Hf_{0.3}Zr_{0.7}O_2$ thin films. This is believed to originate from the decreased crystallinity during the atomic layer deposition (ALD) process due to the lower thermal energy and lower Zr content compared to the $Hf_{0.3}Zr_{0.7}O_2$ films. The ~7.1 nm-thick $Hf_{0.5}Zr_{0.5}O_2$ film deposited at 215 °C showed the highest ESD (~55 J cm^{-3}) with ~57% efficiency at the ~4.94 MV cm^{-1} electric field, and the improved ESD property was analyzed regarding the E_{max} and efficiency. To the authors' knowledge, it is the highest ESD to date for fluorite-structured materials. The high ESD of ~42 J cm^{-3}

with ~62% efficiency could be obtained even after 10^{10} cycles with a ~4.23MV cm^{-1} field amplitude in the ~7.1 nm-thick $Hf_{0.5}Zr_{0.5}O_2$ film deposited at 215 ºC. Moreover, the large ESD was sustained up to 175 ºC without a significant degradation of the ESD and efficiency, which verifies the remarkable thermal stability of the thin film.

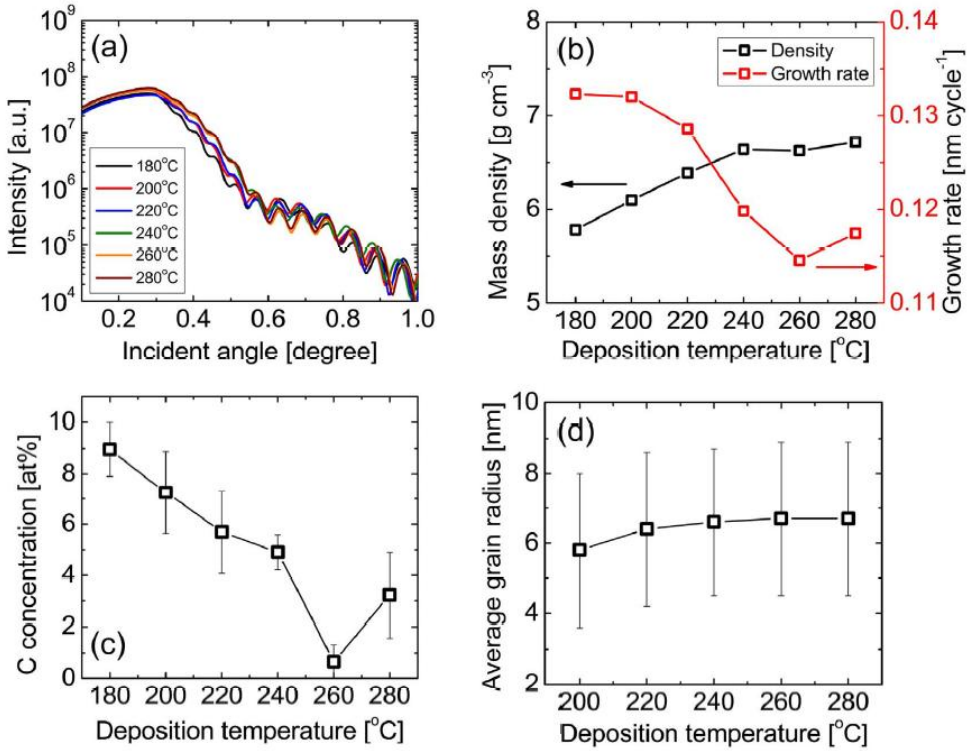

Figure 3.1 (a) X-ray reflectivity pattern of the ~10 nm-thick $Hf_{0.5}Zr_{0.5}O_2$ films deposited at 180–280 °C. (b) Fitted mass density and growth rate (film thickness divided by the number of ALD cycles) of the $Hf_{0.5}Zr_{0.5}O_2$ thin films as a function of T_{dep}. (c) C concentration change from the ~ 10 nm-thick $Hf_{0.5}Zr_{0.5}O_2$ films as a function of T_{dep}. (d) Average grain size of the $Hf_{0.5}Zr_{0.5}O_2$ thin films deposited at 200–280 °C analyzed using a watershed method implemented by the Gwyddion software [39].

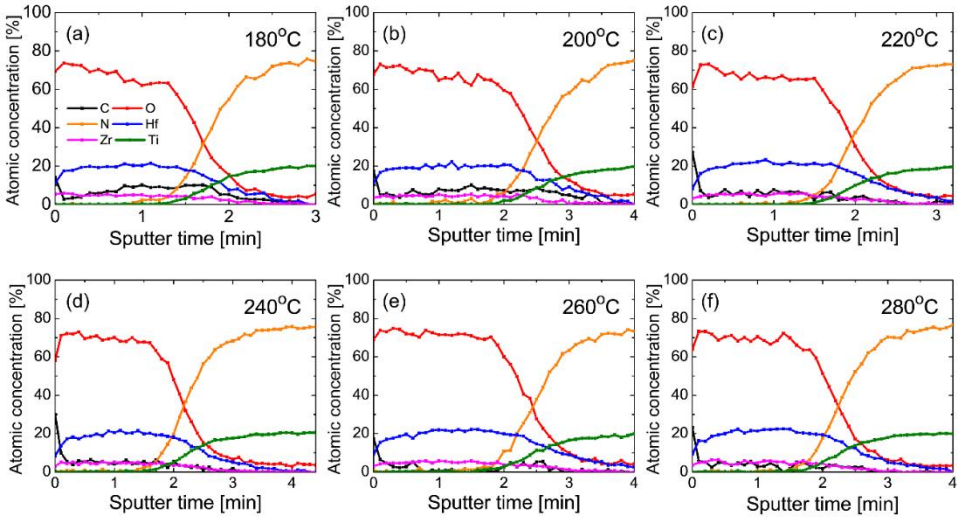

Figure 3.2 Auger electron spectroscopy-depth profiles of the ~10 nm-thick $Hf_{0.5}Zr_{0.5}O_2$ films deposited at (a) 180°C, (b) 200°C, (c) 220°C, (d) 240°C, (e) 260°C, and (f) 280°C.

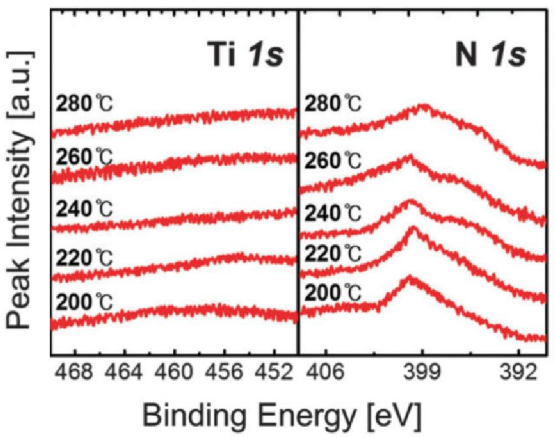

Figure 3.3 XP spectra of the ~9 nm-thick HfO_2 films grown at various T_{dep}s before thermal annealing and top electrode deposition, from the Ti 1s and N 1s orbitals [10].

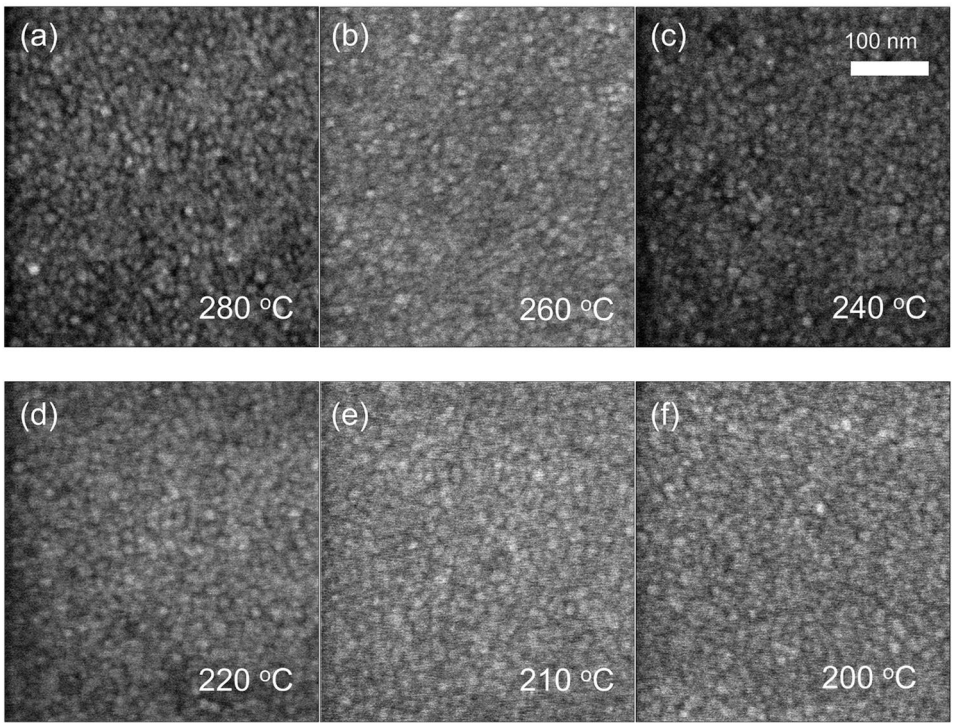

Figure 3.4 Plan-view scanning electron microscopy images of the ~10 nm-thick $Hf_{0.5}Zr_{0.5}O_2$ films deposited at (a) 280°C, (b) 260°C, (c) 240°C, (d) 220°C, (e) 200°C, and (f) 180°C after being crystallized via RTA.

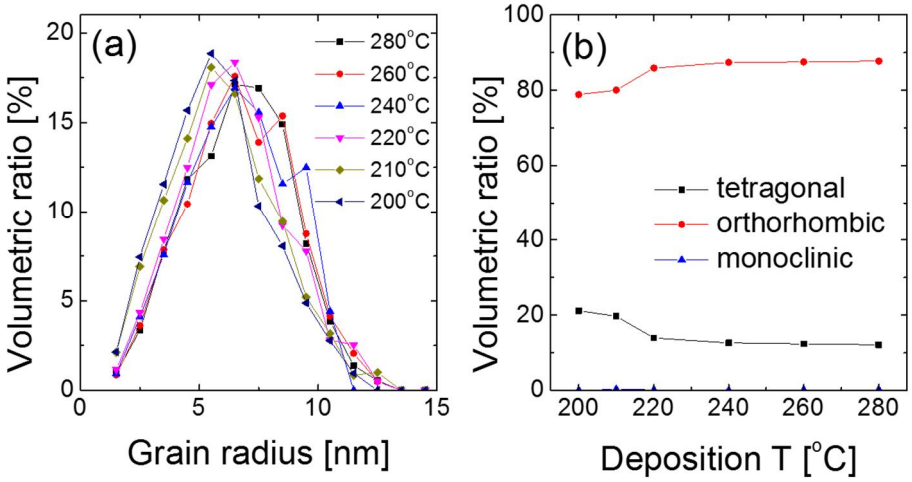

Figure 3.5 (a) Grain size distribution analyzed using the watershed method implemented by the Gwyddion software (Ref. 39 of the main text). (b) Phase fraction with respect to the deposition temperature analyzed from the surface energy model suggested by Materlik and coworkers (Ref. 20 of the main text).

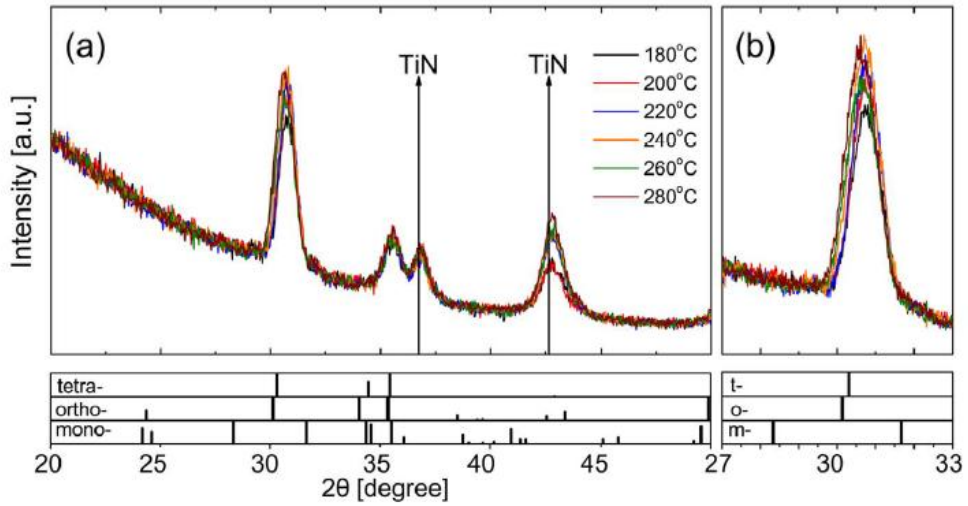

Figure 3.6 (a) Glancing-incidence X-ray diffraction (GIXRD) spectra of the ~10 nm-thick $Hf_{0.5}Zr_{0.5}O_2$ films deposited at 180–280 °C with a 20–50° 2θ range. (b) GIXRD spectra of the $Hf_{0.5}Zr_{0.5}O_2$ films with a 27–33° 2θ range and with a longer acquisition time per step. The powder patterns were obtained from Reference code: 98-017-3966 (tetragonal), 98-006-7004 (orthorhombic), and 98-002-7313 (monoclinic).

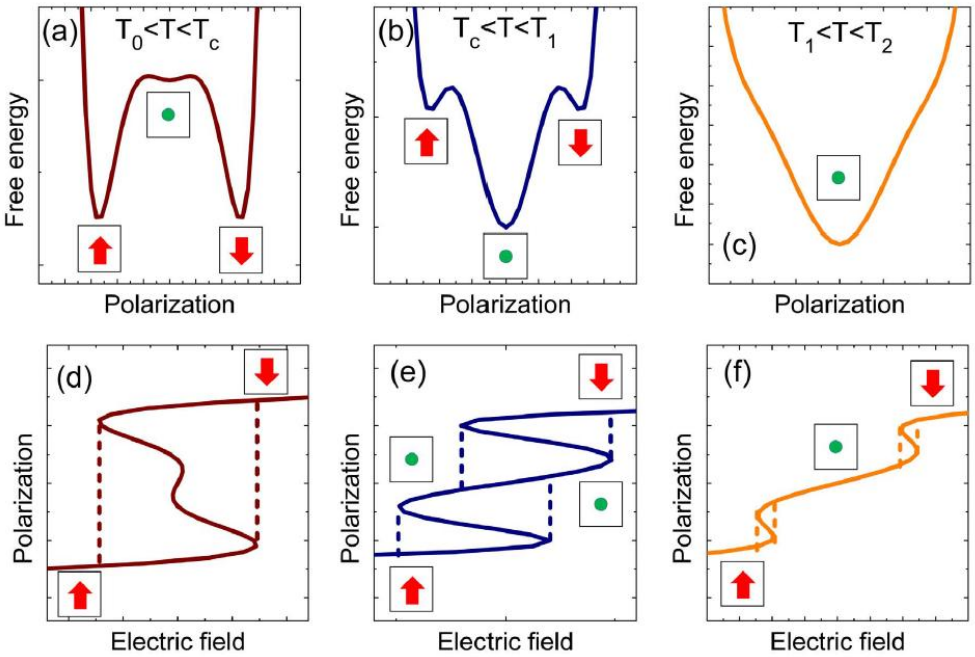

Figure 3.7 Schematic free energy-polarization (F-P) diagram based on the Landau-Ginzburg-Devonshire (LGD) model at the (a) $T_0 < T < T_c$, (b) $T_c < T < T_1$, and (c) $T_1 < T < T_2$ temperatures. Polarization-electric field diagram based on the LGD model at the (d) $T_0 < T < T_c$, (e) $T_c < T < T_1$, and (f) $T_1 < T < T_2$ temperatures (T_0: Curie-Weiss temperature; T_c: Curie temperature; T_1: limit temperature of ferroelectricity; and T_2: limit temperature of field-induced ferroelectricity).

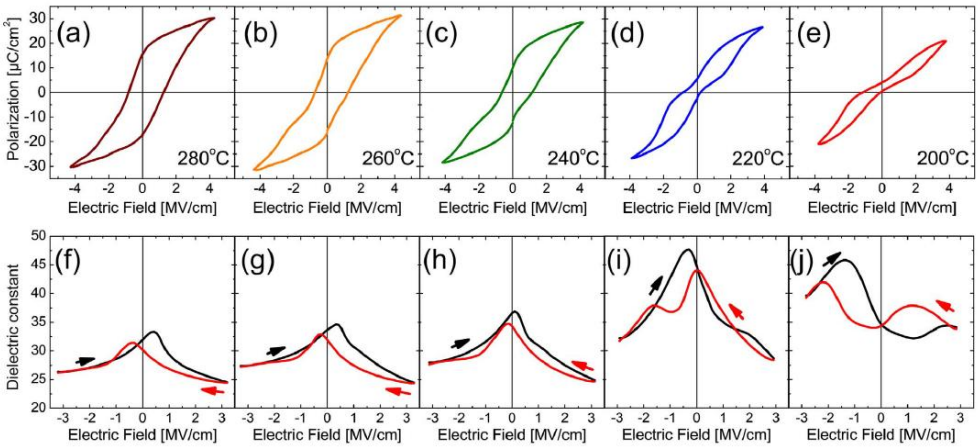

Figure 3.8 Polarization-electric field characteristics of the ~10-nm-thick $Hf_{0.5}Zr_{0.5}O_2$ films deposited at (a) 280 °C, (b) 260 °C, (c) 240 °C, (d) 220 °C, and (e) 200 °C. Dielectric constantelectric field curves of the identical films deposited at (f) 280 °C, (g) 260 °C, (h) 240 °C, (i) 220 °C, and (j) 200 °C.

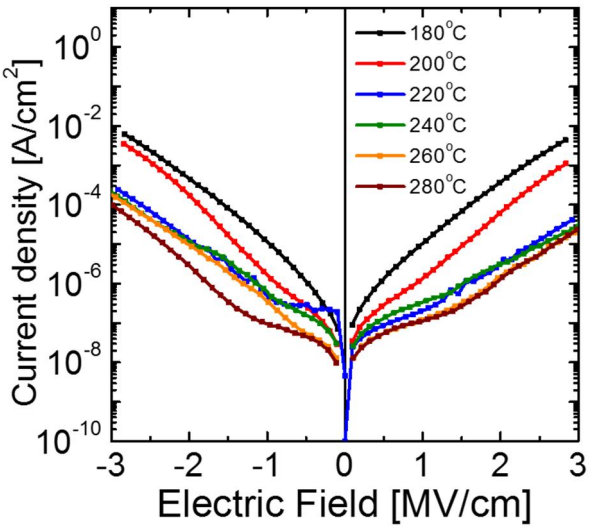

Figure 3.9 Current density-electric field curves of the ~10 nm-thick $Hf_{0.5}Zr_{0.5}O_2$ films deposited at various temperatures.

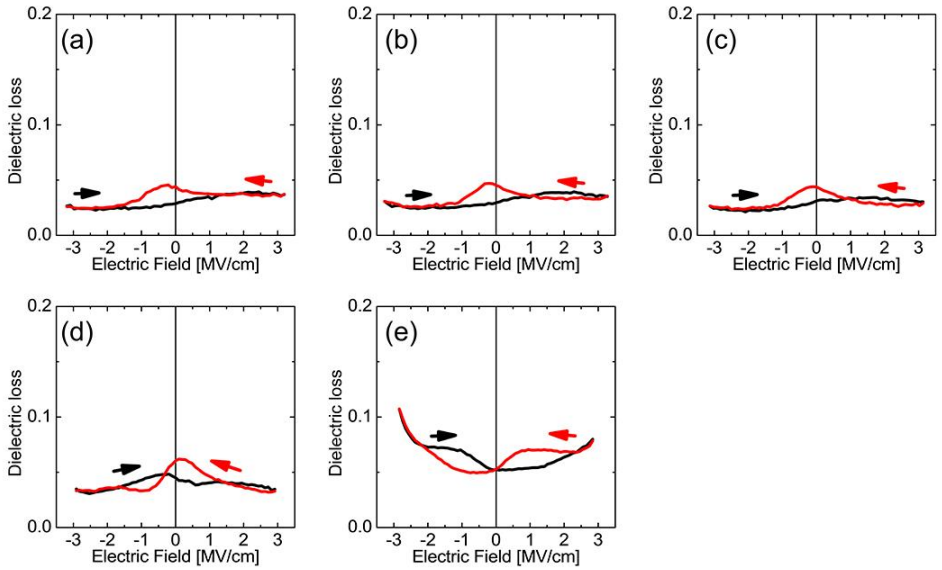

Figure 3.10 Dielectric loss–electric field curves for the ~10 nm $Hf_{0.5}Zr_{0.5}O_2$ thin film capacitors deposited at the (a) 280ºC, (b) 260ºC, (c) 240ºC, (d) 220ºC, (e) 200ºC.

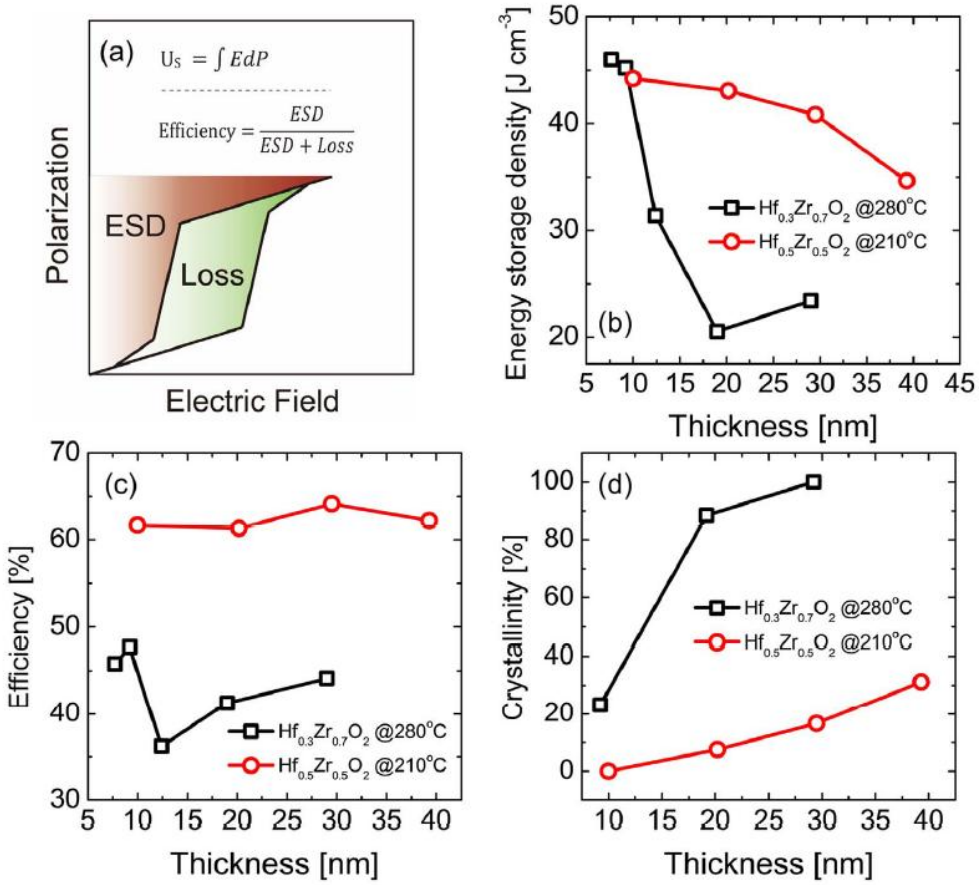

Figure 3.11 (a) Schematic picture illustrating the energy storage behavior in the P-E diagram. (b) Energy storage density, (c) efficiency, and (d) crystallinity compared to the films after RTA as a function of the film thickness for the $Hf_{0.3}Zr_{0.7}O_2$ films deposited at 280 °C (data reproduced from Ref. [49]) and the $Hf_{0.5}Zr_{0.5}O_2$ films deposited at 210 °C.

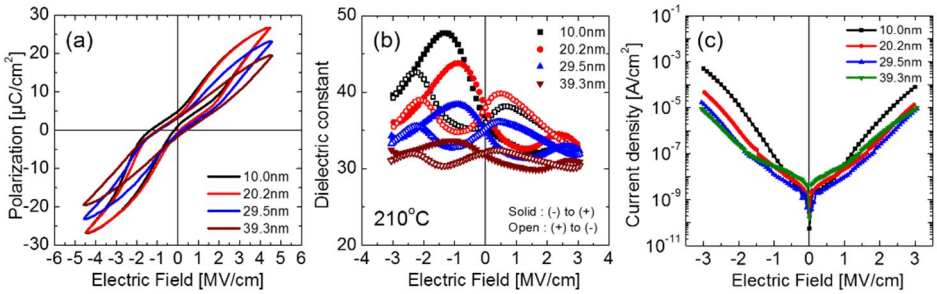

Figure 3.12 (a) Polarization-electric field curves, (b) dielectric constant-electric field curves, and (c) current density-electric field characteristics of the $Hf_{0.5}Zr_{0.5}O_2$ thin films deposited at 210ºC with 10.0, 20.2, 29.5, and 39.3 nm thicknesses.

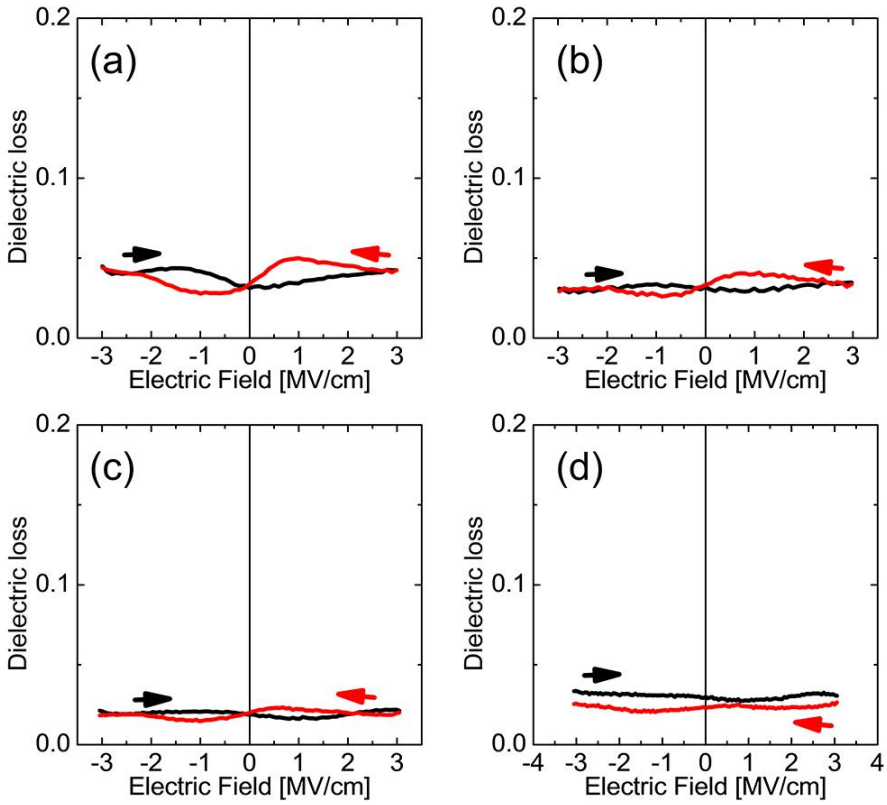

Figure 3.13 Dielectric loss–electric field curves for the $Hf_{0.5}Zr_{0.5}O_2$ thin film capacitors deposited at the 210 ºC with the thickness of (a) 10.0 nm, (b) 20.2 nm, (c) 29.5nm, and (d) 39.3 nm.

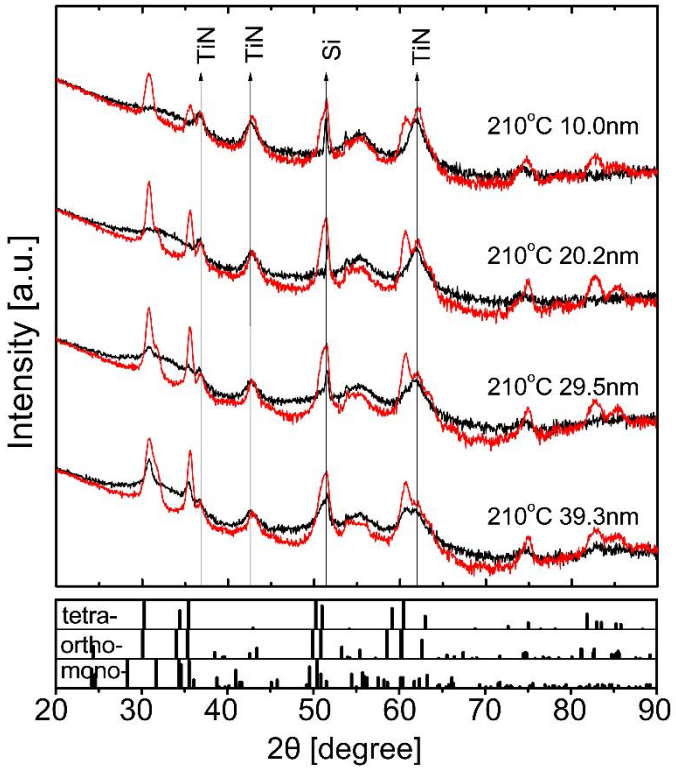

Figure 3.14 Glancing-incidence X-ray diffraction (GIXRD) patterns for the $Hf_{0.5}Zr_{0.5}O_2$ thin films with 10.0, 20.2, 29.5, and 39.3 nm thicknesses as-deposited (black) and crystallized via RTA (red). The powder patterns were obtained from Reference code: 98-017-3966 (tetragonal), 98-006-7004 (orthorhombic), and 98-002-7313 (monoclinic).

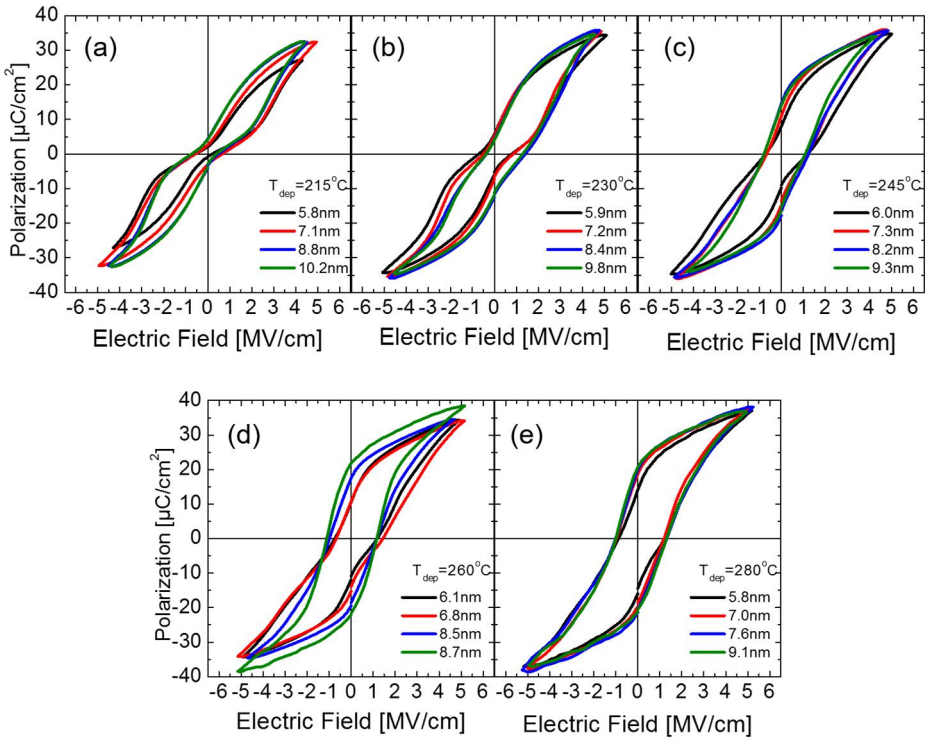

Figure 3.15 Polarization-electric field curves of the $Hf_{0.5}Zr_{0.5}O_2$ thin films deposited at (a) 215 ºC, (b) 230 ºC, (c) 245 ºC, (d) 260 ºC, and (e) 280 ºC with thicknesses within the ~6 - 10 nm range.

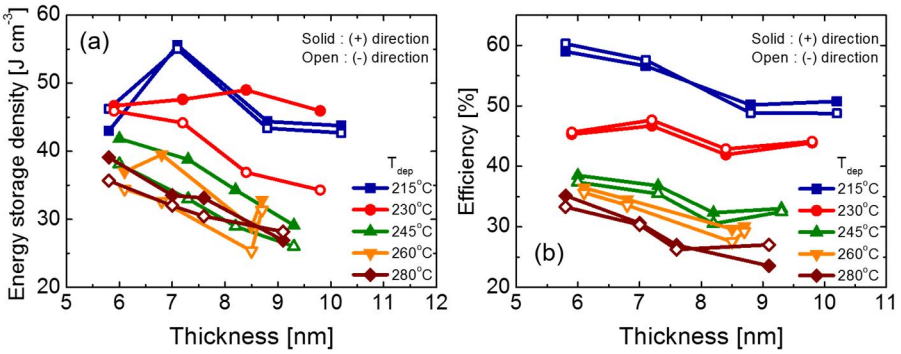

Figure 3.16 (a) Energy storage density and (b) efficiency with a function of the film thickness for the polarization-electric field of the $Hf_{0.5}Zr_{0.5}O_2$ thin films deposited at 215 – 280 ºC shown in Figure 3.15.

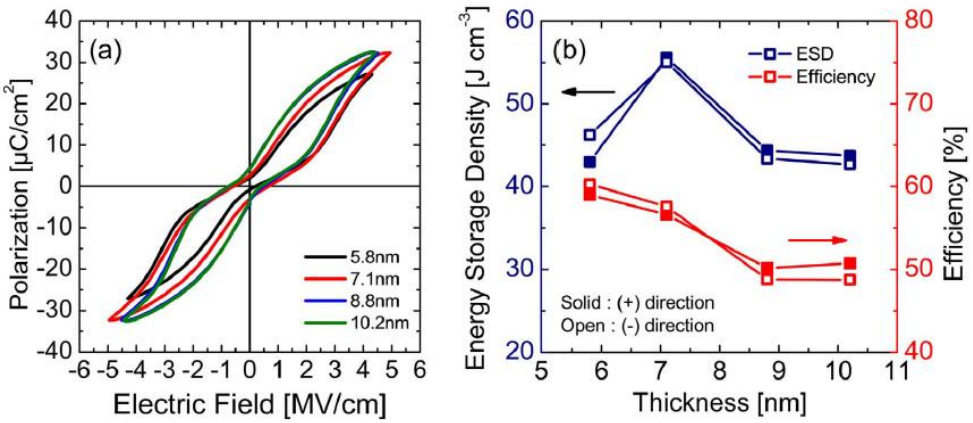

Figure 3.17 (a) Polarization-electric field (P-E) curves for the $Hf_{0.5}Zr_{0.5}O_2$ thin films deposited at 215 °C with 5.8, 7.1, 8.8, and 10.2 nm thicknesses. (b) Energy storage density and efficiency as a function of the film thickness for the polarization-electric field (P-E) curves in (a).

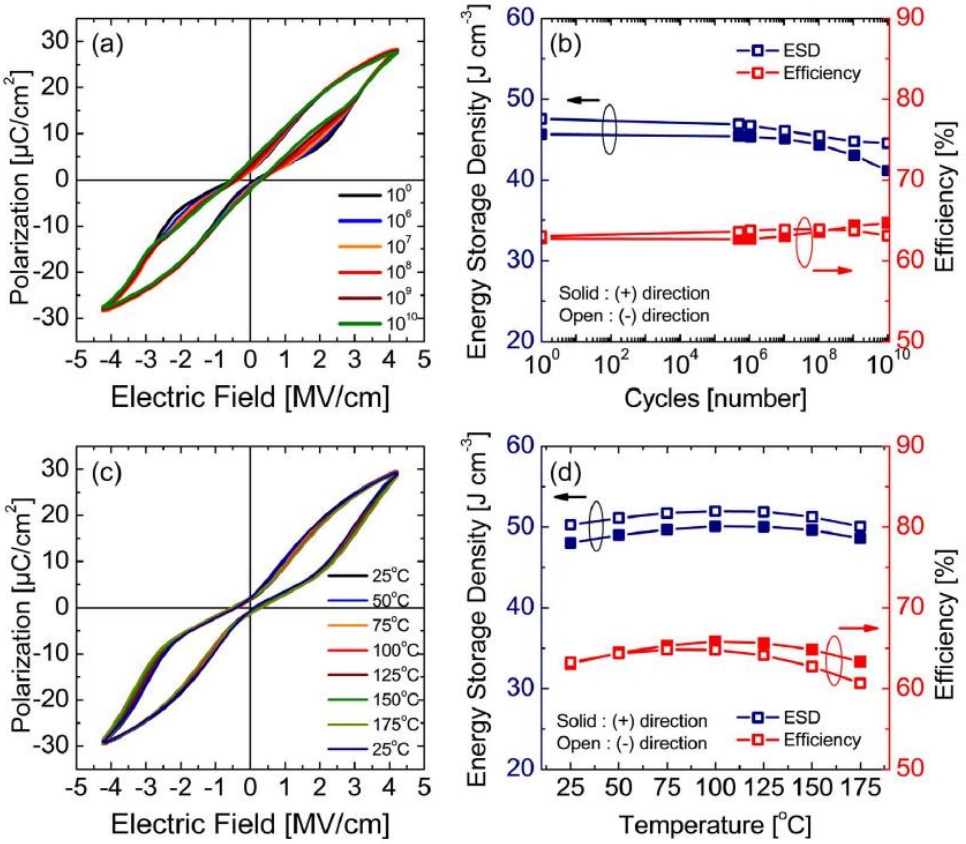

Figure 3.18 (a) Polarization-electric field curves and (b) energy storage density and efficiency for the $Hf_{0.5}Zr_{0.5}O_2$ thin films deposited at 215 °C after bipolar field cycling with a 4.23 MV cm−1 amplitude at a 500 kHz frequency up to 10^{10} cycles. (c) P-E curves and (d) ESD and efficiency for the identical films at various temperatures (from 25 to 175 °C).

3.5. Bibliography

[1] P. Polakowski, J. Müller, *Appl. Phys. Lett*. 106, 232905 (2015).

[2] T. S. Böscke, J. Müller, D. Bräuhaus, U. Schröder, U. Böttger, *Appl. Phys. Lett*. 99102903 (2011).

[3] J. Müller, U. Schröder, T. S. Böscke, I. Müller, U. Böttger, L. Wilde, J. Sundqvist, M. Lemberger, P. Kücher, T. Mikolajick, L. Frey, *J. Appl. Phys*. 110, 114113 (2011).

[4] S. Mueller, J. Mueller, A. Singh, S. Riedel, J. Sundqvist, U. Schroeder, T. Mikolajick, *Adv. Funct. Mater*. 22, 2412 (2012).

[5] S. Mueller, C. Adelmann, A. Singh, S. Van Elshocht, U. Schroeder, T. Mikolajick, *ECS J. Solid State Sci. Technol*. 1, N123 (2012).

[6] T. Schenk, S. Mueller, U. Schroeder, R. Materlik, A. Kersch, M. Popovici, C. Adelmann, S. Van Elshocht, T. Mikolajick, in: *Proceedings of the European Solid-State Device Research Conference (ESSDERC)*, New York, September, p260 (2013).

[7] J. Müller, T. S. Böscke, Y. Yurchuk, P. Polakowski, J. Paul, D. Martin, T. Schenk, K. Khullar, A. Kersch, W. Weinreich, S. Riedel, K. Seidel, A. Kumar, T. M. Arruda, S. V. Kalinin, T. Schlosser, R. Boschke, R. van Bentum, U. Schröder, T. Mikolajick, *Digest Technical papers, in: IEEE International Electron Devices Meeting (IEDM)*, New York, December, 10.8.1 (2013).

[8] S. Starchich, U. Boettger, *J. Mater. Chem. C* 5, 333 (2017).

[9] L. Xu, T. Nishimura, S. Shibayama, T. Yajima, S. Migita, A. Toriumi, *Appl. Phys. Express* 9, 091501 (2016).

[10] K. D. Kim, M. H. Park, H. J. Kim, Y. J. Kim, T. Moon, Y. H. Lee, S. D. Hyun, T. Gwon, C. S. Hwang, *J. Mater. Chem. C* 4, 6864 (2016).

[11] J. Müller, T. S. Böscke, U. Schröder, S. Müller. D. Bräuhaus, U. Böttger, L. Frey, T. Mikolajick, *Nano Lett.* 12, 4318 (2012).

[12] M. H. Park, H. J. Kim, Y. J. Kim, W. Lee, T. Moon, C. S. Hwang, *Appl. Phys. Lett*. 102, 242905 (2013).

[13] M. H. Park, H. J. Kim, Y. J. Kim, W. Lee, H. K. Kim, C. S. Hwang, *Appl. Phys. Lett*. 102, 112914 (2013).

[14] M. H. Park, H. J. Kim, Y.J. Kim, T. Moon, C. S. Hwang, *Appl. Phys. Lett.* 104, 072901 (2014).

[15] O. Ohtaka, H. Fukui, T. Kunisada, T. Fujisawa, *J. Am. Ceram. Soc*. 84, 1369 (2001).

[16] O. Ohtaka, H. Fukui, T. Kunisada, T. Fujisawa, K. Funakoshi, W. Utsumi, T. Irifune, K. Kuroda, T. Kikegawa, *Phys. Rev. B* 63, 174108 (2001).

[17] X. Sang, E. D. Grimley, T. Schenk, U. Schröder, J. M. LeBeau, *Appl. Phys. Lett.* 106, 162905 (2015).

[18] E. D. Grimley, T. Schenk, X. Sang, Milan Pešić, U. Schroeder, T. Mikolajick, J. M. LeBeau, *Adv. Electron. Mater*. 2, 1600173 (2016).

[19] E. H. Kisi, *J. Am. Ceram. Soc*. 81, 741 (1998).

[20] R. Materlik, C. Künneth, A. Kersch, *J. Appl. Phys*. 117, 134109 (2015).

[21] Z. Fan, J. Deng, J. Wang, Z. Liu, P. Yang, J. Xiao, X. Yan, Z. Dong, J. Wang, J. Chen, *Appl. Phys. Lett*. 108, 012906 (2016).

[22] M. H. Park, Y. H. Lee, Kim, H. J. Kim, Y.J. Kim, T. Moon, K. D. Kim, J. Müller, A. Kersch, U. Schröder, T. Mikolajick, C. S. Hwang, *Adv. Mater*. 27, 1811 (2015).

[23] S. E. Reyes-Lillo, K. F. Garrity, K. M. Rabe, *Phys. Rev. B* 90, 140103 (2014).

[24] K. Yao, S. Chen, M. Rahimabady, M. S. Mirshekarloo, S. Yu, F. E. H. Tay, T. Sritharan, L. Lu, *IEEE Trans. Ultrason. Ferr*. 58, 1968 (2011).

[25] M. H. Park, H. J. Kim, Y.J. Kim, T. Moon, K. D. Kim, C. S. Hwang, *Adv. Energy Mater*. 4, 1400610 (2014).

[26] M. Hoffmann, U. Schroeder, C. Künneth, A. Kersch, S. Starschich, U. Böttger, T. Mikolajick, *Nano Energy,* 18, 154 (2015).

[27] M. Pešić, M. Hoffmann, C. Richter, T. Mikolajick, U. Schroeder, *Adv. Funct. Mater*. 26, 7486 (2016).

[28] X. Hao, Y. Wang, L. Zhang, L. Zhang, S. An, *Appl. Phys. Lett*. 102, 163903 (2013).

[29] B. Ma, D.-K. Kwon, M. Narayanan, U. Balachandran, *J. Mater. Res*. 24, 2993 (2009).

[30] T. S. Böscke, St. Teichert, D. Bräuhaus, J. Müller, U. Schröder, U. Böttger, T. Mikolajick, *Appl. Phys. Lett*. 99, 112904 (2011).

[31] H. Yu, C.-C. Chung, N. Shewmon, S. Ho, J. H. Carpenter, R. Larrabee, T. Sun, J. L. Jones, H. Ade, B. T. O'Connor, F. So, *Adv. Funct. Mater*. 27, 1700461 (2017).

[32] P. D. Lomenzo, P. Zhao, Q. Takmeel, S. Moghaddam, T. Nishida, M. Nelson, C. M. Fancher, E. D. Grimley, X. Sang, J. M. LeBeau and J. L. Jones, *J. Vac. Sci. Technol. B* 32, 03D123 (2014).

[33] P. D. Lomenzo, Q. Takmeel, C. Zhou, C. M. Fancher, E. Lambers, N. G. Rudawski, J. L. Jones, S. Moghaddam, T. Nishida, *J. Appl. Phys.* 117, 134105 (2015).

[34] B.-T. Lin, Y.-W. Lu, J. Shieh, M.-J. Chen, *J. Eur. Ceram. Soc*. 37, 1135 (2017).

[35] J. H. Kim, T. J. Park, S. K. Kim, D.-Y. Cho, H.-S. Jung, S. Y. Lee, C. S. Hwang, *Appl. Surf. Sci,* 292, 852 (2014).

[36] X. Liu, S. Ramanathan, A. Longdergan, A. Srivastava, E. Lee, T. E. Seidel, J. T. Barton, D. Pang, R. G. Gordon, *ECS J. Solid State Sci. Technol.* 152, G213 (2005).

[37] H.-S. Jung, S. H. Jeon, H. K. Kim, I.-H. Yu, S. Y. Lee, J. Lee, Y. J. Chung, D.-Y. Cho, N.-I. Lee, T. J. Park, J.-H. Choi, S. Han, C. S. Hwang, *ECS J. Solid State Sci. Technol.* 1, N33 (2012).

[38] D.-Y. Cho, H. S. Jung, I.-H. Yu, J. H. Yoon, H. K. Kim, S. Y. Lee, S. H. Jeon, S. Han, J. H. Kim, T. J. Park, B.-G. Park, C. S. Hwang, *Chem. Mater*. 24, 3534 (2012).

[39] D. Nečas, P. Klapetek, *Cent. Eur. J. Phys*. 10, 181 (2012).

[40] M. E. Lines, A. M. Glass, Principles and Applications of Ferroelectrics and Related Materials, Oxford University Press, New York (2001).

[41] K. M. Rabe, C. H. Ahn, J.-M. Triscone, Physics of Ferroelectrics: A Modern Perspective, Springer, New York (2007).

[42] M. H. Park, H. J. Kim, Y. H. Lee, Y. J. Kim, T. Moon, K. D. Kim, S. D. Hyun, C. S. Hwang, *Nanoscale,* 8, 13898 (2016).

[43] M. H. Park, H. J. Kim, Y. J. Kim, K. D. Kim, Y. H. Lee, S. D. Hyun, C. S. Hwang, *Adv. Mater*. 28, 7956 (2016).

[44] W. J. Merz, *Phys. Rev*. 91, 513 (1953).

[45] M. H. Park, H. J. Kim, Y.J. Kim, T. Moon, K. D. Kim, C. S. Hwang, *Nano Energy,* 12, 131 (2015).

[46] M. H. Park, H. J. Kim, Y. J. Kim, Y. H. Lee, T. Moon, K. D. Kim, S. D. Hyun, C. S. Hwang, *Appl. Phys. Lett.* 107, 192907 (2015).

[47] T. D. Huan, V. Sharma, G. A. Rossetti Jr., R. Ramprasad, *Phys. Rev. B* 90, 064111 (2014).

[48] S. Clima, D. J. Wouters, C. Adelmann, T. Schenk, U. Schroeder, M. Jurczak, G. Pourtois, *Appl. Phys. Lett*. 104, 092906 (2014).

[49] M. H. Park, Y. H. Lee, H. J. Kim, T. Schenk, W. Lee, K. D. Kim, F. P. G. Fengler, T. Mikolajick, U. Schröder, C. S. Hwang, *Nanoscale*, 9, 9973 (2017).

[50] D. M. Hausmann, R. G. Gordon, *J. Cryst. Growth,* 249, 251 (2003).

[51] N. Umezawa, K. Shiraishi, T. Ohno, H. Watanabe, T. Chikyow, K. Torii, K. Yamabe, K. Yamada, H. Kitajima, T. Arikado, *Appl. Phys. Lett.* 86, 143507 (2005).

[52] R. Suzuki, N. Taoka, M. Yokoyama, S.-H. Kim, T. Hoshii, T. Maeda, T. Yasuda, O. Ichikawa, N. Fukuhara, M. Hata, M. Takenaka, S. Takagi, *J. Appl. Phys.* 112, 084103 (2012).

[53] S. V. Elshocht, M. Caymax, S. D. Gende, T. Conard, J. Petry, L. Date, D. Pique, M. M. Heyns, *ECS J. Electrochem. Soc*. 151, F77 (2004).

[54] L. Kang, B. H. Lee, W.-J. Qi, Y. Jeon, R. Nieh, S. Gopalan, K. Onishi, J. C. Lee, *IEEE Electron Device Lett*. 21, 181 (2000).

[55] P. P. Apte, K. C. Saraswat, *IEEE Trans. Electron Devices* 41, 1595 (1994).

[56] D. Zhou, J. Xu, Q. Lu, Y. Guan, F. Cao, X. Dong, J. Müller, T. Schenk, U. Schröder, *Appl. Phys. Lett*. 103, 192904 (2013).

4. Transient negative capacitance effect in the atomic-layer-deposited $Al_2O_3/Hf_{0.3}Zr_{0.7}O_2$ bilayer thin film

4.1. Introduction

The negative capacitance (NC) effect using the suppression of the spontaneous polarization of the ferroelectric (FE) material is now attracting a great deal of interest as a strategy to achieve extremely large capacitance density or the subthreshold swing of sub-60mV/decade in field effect transistors [1-6]. The capacitance enhancement in the ferroelectric/dielectric (FE/DE) bilayer larger than the capacitance of the constituent DE layer was suggested as an evidence of the occurrence of the static NC effect in the FE/DE bilayer system [7-9], which was first reported in the epitaxial-$Pb(Zr_{0.2}Ti_{0.8})O_3/SrTiO_3$ (PZT/STO) capacitor at a temperature higher than 573K in 2011 [7]. The similar capacitance enhancement effect was reported in the epitaxial-$BaTiO_3/SrTiO_3$ (BTO/STO) capacitor at room temperature in 2014 [8]. It was argued that such negative state of the FE layer capacitance (C_{FE}) in the FE/DE bilayer system could be achieved by inducing the suppression of the spontaneous polarization in the FE layer, which was related to the strong electrostatic coupling between FE and DE layers [7,10]. The unscreened spontaneous polarization charge by the intervened DE layer between FE and electrode layers can induce a significant depolarization field across the FE layer, which involved the corresponding internal field in the DE layer. The two electric fields have opposite directions, and the depolarization field in the FE layer must have an opposite direction to the applied field direction. Therefore, the

total field in the DE layer must be higher than the externally applied field [11,12], which could increase the overall capacitance of the FE/DE layer to a value higher than that of a single DE layer. The insulating property of the DE layer was considered important in limiting the inflow of the compensating charges towards the FE/DE interface during the observation of the NC effect [12]. NC-field effect transistor (NC-FET) is an another intensively studied application that exploits the NC effect, where the semiconductor layer can be considered equivalent to the DE layer in the FE/DE bilayer [1,13-16]. In this application, the internal field exerted by the spontaneous polarization can amplify the gate voltage (voltage amplification effect), thereby achieving the subthreshold swing lower than the Boltzmann limit (60 mV/decade at room temperature).

However, most of these basic arguments lack the careful consideration of the very fundamental aspect of the FE layer, domain formation, which has been regarded as the highly feasible route to alleviate the depolarization field effect. Therefore, the domain formation hampers the static NC effect but only allows transient NC effects being accompanied with serious hysteresis [11,12]. Moreover, the highly nonlinear charge-voltage relationship of the semiconductor also complicates the fundamental understanding of this intriguing effect. The most recent theoretical modelling work from the author reveeealed that, it was almost impossible to achieve the hysteresis-free NC effect in NC-FET based on the load-line analysis [17]. Therefore, this work focuses on the stacked layer of a FE layer and a DE layer (not semiconductor layer).

Another critical problem in the field is as follows: to date, the observation of the static NC effect has been limited to the epitaxial-FE/DE bilayers based on the perovskite structure. These materials are not compatible with the current complementary metal oxide semiconductor (CMOS) technology, even when the FE/DE bilayer is exploited as a dielectric layer for high capacitance capacitor in dynamic random access memory (DRAM). The materials must be grown on a polycrystalline electrode (such as TiN)/Si substrate with either polycrystalline or amorphous structure to be CMOS-compatible. Since the FE layer cannot be amorphous to show the FE performance, it should be polycrystalline. On the other hand, the DE layer could be amorphous. In fact, such a combination of the polycrystalline high-*k* layer (ZrO_2) and the amorphous insulating layer (Al_2O_3) has already been in the mass production with the $ZrO_2/Al_2O_3/ZrO_2$ (ZAZ) format in DRAM capacitor. Therefore, if the ZrO_2 layer can be replaced with an appropriate FE layer, such as $(Hf,Zr)O_2$ in this work, and can show the feasible charge-boosting effect, it will be a great step forward in this field.

In this regard, the authors' recent report on the transient NC effect in the $Al_2O_3/BaTiO_3$ (AO/BTO) bilayer capacitor is notable [18]. In the report, the spontaneous polarization of the homogeneously imprinted FE layer could be reversed with a short external voltage application ($< \sim 1$ μs), which then returned to its original polarization direction when the applied voltage was removed [18]. This means that the epitaxial BTO layer did not switch via the domain mechanism even under the reversing field application, otherwise, the FE state will not go back to the original

state when the field is removed. In this operation, the interfacial charge density, which has been presented in the pristine state to compensate for the FE bound charge of the FE layer, must be invariant [18]. Otherwise, the sample showed a tunnel-switch related FE switching but not the NC effect, which was reported when the sample was tested by a standard polarization – voltage (P-V) meter with a testing timescale as long as ms [11,19]. In this sample, the polarization of the epitaxial BTO was aligned towards the top surface direction due to the several electrostatic origins, such as gradual stress relaxation from the substrate ($SrRuO_3$/$DyScO_3$) along the surface-normal direction, the asymmetric surface chemical state, or the charged defect alignment, which induced a strong imprint effect towards the positive bias direction in its P-V curve [18]. When the thin AO layer was grown on top of the BTO film, the positive bound charge of the BTO layer was compensated by the trapped electrons at the AO/BTO interface, which could be understood from the strongly shifted capacitance-voltage curve (C-V) of the AO/BTO layer toward the positive bias direction. While the C-V curve did not show any capacitance enhancement effect, due to the charge exchange and full compensation of the FE bound charge by the long timescale of the C-V, a pulse-type switching test revealed that the AO/BTO could show a higher capacitance than the single AO layer under the limited conditions. Here, the limited conditions referred to the followings; first, the applied voltage direction must be opposite to the original polarization direction of BTO. Otherwise, there will be no change in the polarization upon the voltage application. Second, the voltage pulse length and height should be short and low not to change the interface trapped charges. Otherwise, the BTO layer permanently switches, and no charge (and

capacitance) boosting could be achieved when the bias is removed. While this was a critical contribution to the fundamental understanding in this field using an amorphous DE layer (Al_2O_3), the adoption of an epitaxial BTO layer was still a critical huddle for its practical application to semiconductor devices.

In this work, the transient NC effects in the amorphous-Al_2O_3/polycrystalline-$Hf_{0.3}Zr_{0.7}O_2$ bilayer systems prepared by using the atomic layer deposition (ALD) method with the CMOS-compatible TiN bottom electrodes are reported in detail. It has been well reported that the solid solution system of polycrystalline HfO_2-ZrO_2 shows intriguing performances depending on the cation composition and film thickness; films with Hf-rich, 50:50 of Hf:Zr, and Zr-rich showed dielectric, ferroelectric, and antiferroelectric properties, respectively, at a typical thickness of ~10 nm [20,21]. Therefore, the natural selection for the FE layer in the AO/(Hf,Zr)O_2 system for this work could have been $Hf_{0.5}Zr_{0.5}O_2$ thin film. However, as can be seen in Figure 4.1, the AO/$Hf_{0.5}Zr_{0.5}O_2$ thin film showed almost symmetrical P-V and C-V curves showing that the FE domains within the polycrystalline film have random orientations. This means that there can hardly be any significant development of the depolarization effect within the FE layer, so there is no need to involve the internal field even when the AO layer was deposited on top. As discussed above for the AO/BTO case, this type of sample is inappropriate for the purpose of this work, because the randomly oriented domains with no preferred polarization direction can self-mitigate the depolarization effect, which should have been induced by the interference of the FE bound charge compensation from the metal electrode by the

presence of the intervened AO layer. Therefore, a different thin film ($Hf_{0.3}Zr_{0.7}O_2$) was adopted in this work although its maximum remanant polarization (P_r) is slightly lower. Detailed characterization results on the $Hf_{0.3}Zr_{0.7}O_2$ film are included in Figure 4.2. The as-deposited $Hf_{0.3}Zr_{0.7}O_2$ film has lower crystallinity due to the low ALD temperature (~280 ^oC), and thus, it is annealed by the rapid thermal annealing (RTA) method before and after the top Pt electrode deposition. The former and latter are referred to as the post-deposition annealing (PDA) and post-metallization annealing (PMA), respectively, and they showed distinctive P-V and C-V properties as shown in Figure 4.2a and b. The PMA sample showed a pinched P-V hysteresis loop, which is a characteristic feature of the antiferroelectric phase (tetragonal phase) of Zr-rich $(Hf,Zr)O_2$. In contrast, the PDA sample showed a typical ferroelectric P-V loop ($2P_r$ ~ 0.21 C m^{-2}) with a rather strong imprint to the positive bias direction. These features could also be confirmed from their respective C-V graphs. Such a difference in the switching and dielectric properties is attributed to the different grain evolution during RTA with and without the capping top electrode. The possible origin on these aspects is presented below.

In this study, the post-deposition annealing (PDA) condition was adopted for crystallization heat treatment of the HZO thin film instead of the post-metallization annealing (PMA) in order to prevent the potential generation of the leakage path in the DE layer during the PMA process. The electrical and the structural changes by the PDA process were compared with those by the PMA condition. Figure 4.2a shows that the field-induced FE in the P-E response transformed almost to the FE response

when the crystallization condition changed from PMA to PDA. Similar electrical property changes can be observed in the small signal AC capacitance-voltage response in Figure 4.2b, where the two capacitance peaks from the field-induced FE response almost transformed to the FE response of one (imprinted) peak at each bias sweep. This can be understood by the top encapsulation effect on the metastable orthorhombic phase (space group $Pca2_1$; o-phase) which is the ferroelectric phase of the HZO thin film. The top encapsulation effect indicates the upper layer has a significant influence on the HfO_2 thin film during the crystallization stage, and it is generally known to kinetically suppress the formation of the monoclinic phase (space group $P2_1/c$; m-phase) stable at room temperature. In other words, the tetragonal phase (space group $P4_2/nmc$; t-phase) cooled from the high-temperature crystallization annealing process can have a driving force for the phase transition to the m-phase stable at room temperature, but the accompanying volume expansion (~131Å^3 for the two-fold unit cell of the t-phase ➔ ~138Å^3 for the m-phase) can be kinetically suppressed by the upper layer, thereby inhibiting the formation of the m-phase. The change of the HZO thin film in Figure 4.2a and b can be understood from the identical mechanism when it is extended for t- and o-phases. In the Zr-rich HZO thin films used in this work, the m-phase is already destabilized by the large Zr composition, and then the t-phase and the o-phase compete for their similar stabilities. As the unit cell volume of the o-phase (~133Å^3) is slightly larger than that of the t-phase, the phase transition to the o-phase can be more facilitated in the absence of the upper layer during the cooling of the thin film, thereby further increasing the o-phase fraction in the thin film.

Therefore, the PDA sample showed the desirable characteristics for the purpose of this work – it had preferred ferroelectric polarization pointing toward the film surface. Figure 4.2c showed the grazing angle incidence X-ray diffraction (GIXRD) patterns of the 10nm-thick $Hf_{0.3}Zr_{0.7}O_2$ and $Hf_{0.5}Zr_{0.5}O_2$ films before and after the top AO layer deposition. The $Hf_{0.5}Zr_{0.5}O_2$ film showed non-negligible contribution from the non-ferroelectric monoclinic phase (denoted as m(-111) and m(111) peaks at 2θ of ~28.5° and ~31.6°) whose intensity slightly increased when the AO layer was deposited, in addition to the desired peak at 2θ of ~30.5° (mixed peak by the ferroelectric orthorhombic and antiferroelectric tetragonal phases). In contrast, the $Hf_{0.3}Zr_{0.7}O_2$ film showed no intensity at the 2θ values of monoclinic phase with a stronger peak intensity at the desired 2θ of ~30.5°. The peaks did not show any notable change upon the AO layer deposition, suggesting the superior structural stability of this material over the $Hf_{0.5}Zr_{0.5}O_2$ film. Figure 4.2d shows the cross-section high-resolution transmission electron microscopy (HRTEM) image of the Pt/7nm-thick AO/10nm-thick $Hf_{0.3}Zr_{0.7}O_2$ film grown on the TiN bottom electrode. The AO and $Hf_{0.3}Zr_{0.7}O_2$ layers have amorphous and polycrystalline structures, respectively, with a well-defined interface structure. These electrical and structural characterization results provided a feasible justification to use the PDA $Hf_{0.3}Zr_{0.7}O_2$ film for confirming the transient NC effect from the stacked layers in this work. For a thorough and systematic study, the AO layer thickness was varied to 5, 7, and 10 nm by varying the ALD cycle numbers (0.1nm/cycle for AO growth).

Because of the preferred and imprinted ferroelectric performance of the $Hf_{0.3}Zr_{0.7}O_2$ layer in the stacked structure, the standard Landau-Ginzburg-Devonshire (LGD) theory for the charge – voltage response can be used [22]. Based on this theory, the transient charge – voltage characteristics could be interpreted based on the previously established transient NC theory. Also, the role of the interface charge during the bilayer deposition process could be understood for the optimum low voltage operation, which needs to remain as small as possible. With the duration change and the repetition of the applied voltage, it was also confirmed that the limitation of the charge injection through the DE layer is essential for the stable NC operation.

4.2. Experimental

The ~10 nm-thick $Hf_{0.3}Zr_{0.7}O_2$ thin films were deposited via thermal atomic layer deposition (ALD) process on a TiN bottom electrode at 280 ºC. $Hf[N(C_2H_5)CH_3]_4$, $Zr[N(C_2H_5)CH_3]_4$, and ozone with 180 g m^{-3} concentrations were used as Hf precursor, Zr precursor, and an oxygen source, respectively. A total 80 cycles of the Hf and Zr precursors with 3:7 cycle ratio yielded the film thickness of ~10 nm. The PDA was performed by the RTA at 500 ºC for 20 s in an N_2 atmosphere to crystallize the $Hf_{0.3}Zr_{0.7}O_2$ thin films. After crystallization, the 5-10 nm-thick Al_2O_3 thin films were deposited via another thermal ALD process using $Al_2(CH_3)_6$ (Al precursor; TMA) and ozone at 250 ºC. Circular Pt top electrodes were fabricated using the e-beam evaporation method with a shadow mask with an area of 15,000 μm^2. Detailed fabrication and the structural analysis methods can be found elsewhere [18,22]. The P-V and the capacitance-electric field (C-E) were measured using a ferroelectric tester (Aixacct Systems, TF Analyzer 2000) at 1 kHz and an impedance analyzer (HP4194A, Hewlett Packard) with 50 mV AC field and 10 kHz AC field frequency, respectively. A pulse generator (Agilent 81110A/81111AW, Agilent) and a digital oscilloscope (TDS684C, Tektronix) were used for the pulse measurement. The top electrode was used to bias the capacitor while the bottom electrode was grounded during the measurements. The X-ray diffractometer (XRD, PANalytical, X'Pert Pro) was used with a GIXRD mode (incidence angle = 0.5 º). The cross-sectional microstructures were analyzed using a HRTEM (JEM-2100F, JEOL Ltd., field emission, 200 kV).

4.3. Results and Discussions

Figure 4.3a shows the P-V loop changes of the 10 nm-thick $Hf_{0.3}Zr_{0.7}O_2$ (HZO) thin films with and without the layered 5, 7, and 10nm-thick AO thin films (Pt top electrode). The P-V loop of AO/HZO bilayer with thinner Al_2O_3 layer (~1.8 nm) was presented in Figure 4.4a. While the single HZO layer showed a typical imprinted ferroelectric hysteresis loop as already discussed above, the samples with the different AO layers did not show any hysteresis but just linear P-V graphs. This is very distinctive from the PMA-treated AO/$Hf_{0.5}Zr_{0.5}O_2$ thin films shown in Figure 4.1a, where the AO thickness was ranged from 2.3 to 8.1 nm. As discussed above, the emergence of the hysteretic P-V curve in the AO/HZO film indicates the tunnel-switch effect, i.e., the AO layer was electrically leaky to allow the interface charge exchange upon the polarization switching of the HZO layer, meaning that the NC effect was readily hampered. This was believed to be due to the increased leakage through the AO layer which must be induced by RTA during the PMA process. It should be noted that the decrease of remanent polarization and hysteresis of the AO/$Hf_{0.5}Zr_{0.5}O_2$ bilayers with the increasing AO thickness is not related with the indication of transition to NC state, where the free energy of DE layer dominates over the one of FE layer. Such transition can hardly be distinguished from the slow P-V test especially for NC state with transient nature because any P_s switching even in NC state can be measured as general P_r due to the (bound) charge injection. The decrease of switchable polarization in Figure 4.1 is considered more related with simply

inefficient (bound) charge movement through AO layer with the increase in AO thickness.

However, the linear P-V in Figure 4.3a for the case of the samples comprised of non-annealed AO layer on the PDA-HZO film indicates that the AO layer retained highly insulating property, inhibiting the interfacial charge exchange even at such a slow P-V test process. This is an important feature of the samples adopted in this work. Otherwise, most of the transient NC effect reported in this work would have been hampered by the high leakage through the thin AO layer. Figure 4.3b shows the small-signal C-V response of the 5-10 nm-thick AO/HZO bilayer thin films. The single layer HZO film showed the highest capacitance density with a significant hysteresis, which is consistent with the P-V hysteretic behavior in Figure 4.3a. Other AO/HZO films showed negligible hysteresis with lower capacitance density than the respective AO layers (indicated by the lateral dotted lines) suggesting that the two layers in each sample work as the normal dielectric layer. The thickness of the constituent AO layer was electrically estimated by the total capacitance values (C_{tot}) near 0 V and the dielectric constant of 8.9 for the amorphous AO layer, and the capacitance value of HZO layer (C_{HZO}) which was taken as the value of non-switching state (~2.6 μF cm^{-2}) using the equation of $C_{AO} = ({C_{tot}}^{-1} - {C_{HZO}}^{-1})^{-1}$. The calculation yields the electrical AO thickness of the 5, 7, and 10nm-thick AO/HZO bilayers as 5.5±0.4, 7.3±0.6, and 10.1±0.6 nm, respectively, where the physically estimated AO layer thickness from the X-ray reflectance was 5.6±0.6, 6.7±0.4, and 9.7±0.4 nm, respectively. These values are in feasible coincidence suggesting the

reasonable interpretation of the electrical data. These electrical AO thicknesses also well explain the decreasing slope of the linear P-V graphs in Figure 4.3a with the increasing AO thickness. Figure 4.3c shows the GIXRD patterns of the HZO thin films before and after the deposition of the 10nm-thick AO layer. Since the intensity of the orthorhombic (111)/tetragonal (011) peak near 30.5° was almost unchanged with no evolution of the monoclinic peak near 28.5° and 31.6°, the deterioration of the thin film by the evolution of the parasitic monoclinic phase can be considered to be hardly occurred. These findings indicate that the interface between the AO and HZO layers already contained interfacial trap charge (σ_i), which can compensate for the ferroelectric polarization charge of the HZO film, making HZO well polarized. Due to the very insulating nature of the AO layer, σ_i did not vary upon the DC voltage sweep during the P-V and C-V tests. This is in a stark contrast to the case of AO/BTO case or AO/$Hf_{0.5}Zr_{0.5}O_2$ case in Figure 4.1, where the σ_i varies along with the DC voltage making the P-V and C-V hysteretic with apparently higher coercive voltage values.

Since the standard low-frequency C-V tests did not show any possibility for the involvement of the charge boosting effect, a short-pulse type charge – voltage test was performed. Figure 4.5a shows the charging/discharging current peaks when a 500 ns square pulse bias is applied to the 10 nm-thick AO/HZO bilayer capacitor as an example. The inset in Figure 4.5a is the equivalent circuit of the measurement set-up. The leakage current was small as observed in the negligible current in response to prolonged voltage application after initial charging peak in Figure 4.5a, and the charge density identical amplitude with the flat (leakage) currents in charging and

discharging regions were excluded in the plot of Figure 4.5e and f below. The charging charge density (Q_c) and the discharging charge density (Q_{dis}) can be obtained by integrating the charging and discharging current peaks, respectively, and the residual charge (Q_{res}) is the difference between the two values (Q_c-Q_{dis}). Figure 4.5b compares the charge density-voltage curves obtained from the pulse measurement and the AC capacitance measurement at 10 kHz in the low voltage regions of the 5-10 nm-thick AO/HZO bilayer capacitor. The capacitance densities obtained from the two measurements are almost identical, demonstrating the validity of the measurement set up, which was also examined in the previous study [18]. Figures 4.5c and d show the charge density-voltage plot for the negative and positive bias conditions of the ~10 nm-thick HZO single layer capacitor in the pristine state. The residual charge does not increase down to a voltage of -2.5V in Figure 4.5c and up to +4V in Figure 4.5d due to no operation of the P_s switching. The higher voltage of such operation in the positive bias region coincided with the positively imprinted P-V shape of the single layer HZO capacitor shown in Figure 4.3a. It should be noted that these voltages (-2.5V and +4V) do not necessarily coincide with the critical voltage (~2V) for the hysteresis formation in the subloop P-V test in Figure 4.6 due to the measurement frequency difference. When the pulse voltage was lower than -2.5V and higher than +4V in the respective figures, the Q_{res} increased suddenly due to the operation of the P_r reversal, which kept the input charge inside the capacitor even when the voltage was removed. In contrast, the 10 nm-thick AO/HZO bilayer thin film in Figure 4.5e showed a distinctively different behavior. First, the estimated Q_{res} remained almost zero up to the highest test voltage (17V), suggesting that either

P_r did not switch at all or it recovered the original state when the voltage was removed. When the voltage was lower than ~12V, the Q_c and Q_{dis} curves showed almost linear variation with the applied voltage, of which the slope corresponds to the capacitance value achieved from the C-V test shown in Figure 4.3b. This suggests that the stacked layer just played the role of two serially connected positive capacitors. However, at voltages > ~12 V, the slope suddenly increased, of which slope corresponded to a capacitance higher than that of the single layer 10nm-thick AO layer (which is represented by the black solid line in the graph). Therefore, this phenomenon implied that there was a charge boosting effect involved possibly by the reversible motion of P_r of the HZO layer under this condition. It should be reminded that the single layer HZO layer showed a significant value of Q_{res} when P_r responded to the voltage stimuli in Figure 4.5c and d. Therefore, as for the AO/BTO (epitaxial) case, the charge boosting, and thus, transient NC effect of the polycrystalline HZO might be involved in this short-pulse experiment.

Figure 4.5f plots the discharge density-voltage curves (dot) of the 5-10 nm-thick AO/HZO bilayers and their fitted lines based on the LGD model (dotted lines) applied to the HZO layer. The details of the LGD fitting process will be discussed in more detail later in the main text and in SI. The high coincidence between the theoretical model and experimental results revealed that such charge boosting effect must be ascribed to the reversible motion of the FE polarization in the HZO layer. The maximum allowable voltage (V_{max}) for each thickness was limited to the range where the hard breakdown or the increase of the Q_{res} does not occur. The almost identical V_{max} could be observed for the sufficiently large number of different capacitors at

each sample with different AO layer thicknesses. The onset voltage of the charge boosting (or capacitance enhancement) was relatively blurred compared to that of the epitaxial BTO material in the previous report [18]. This could be attributed to the random orientation characteristic of the grains of the polycrystalline HZO thin film. Nonetheless, it will be shown that the fitting of the curves with different AO thicknesses could be achieved by the LGD model using a single set of the fitted Landau coefficients for the HZO thin film (see next).

The electric displacement of the HZO thin film can be expressed as follows considering the (almost) random orientation of the thin film.

$$\widehat{D} = \frac{1}{4\pi}\iint_A D \cdot \dot{n} dA = \frac{3}{4}\varepsilon_0 \varepsilon_{\frac{\Sigma}{3}} E_{tot,f} + \frac{1}{2}P_s$$
$$= \frac{3}{2}\varepsilon_0 \varepsilon_{\Sigma/3}(\alpha P_s + \beta {P_s}^3 + \gamma {P_s}^5) + \frac{1}{2}P_s \quad (4.1)$$

$\widehat{D}$, D, $\dot{n}$, ε_0, $\varepsilon_{\Sigma/3}$, P_s, and $E_{tot,f}$ indicate the electric displacement to the interface-normal direction, arbitrary electric displacement vector in the orthorhombic crystal structure, vector of the spherical direction, vacuum permittivity, dielectric constant of HZO, spontaneous polarization of HZO, and the total electric field applied on the HZO layer, which is the sum of the external and depolarization fields, respectively. α, β, and γ are the Landau coefficients. The dielectric constant of HZO is obtained from the lower value of the capacitance density at 0V in Figure 4.3b, which was ~24, to eliminate the contribution of polarization switching while 8.9 was

used for the dielectric constant of the AO layer according to the previous literatures [18,23]. The random orientation was dealt through the inculcation of the isotropic average method for the electric displacements at each axial direction of the HZO unit cell, where P_s appears only in the z-axis direction of the orthorhombic crystal structure according to the first principle calculation [24,25]. Higher order of interactions between the axes were neglected considering their sufficiently small contributions. Finally, the partially imprinted state was expressed by changing the sign of σ_i.

$$D_{tot}(\mathrm{V}) = (1-\delta)\cdot D_{up(\sigma_i)}(\mathrm{V}) + \delta \cdot D_{down(-\sigma_i)}(\mathrm{V}) \tag{4.2}$$

The δ term represents the domain fraction of the thin film, where the overall P_s direction is consistent with the external field direction. The detailed derivation process and the fitting parameters for the electrostatic model are summarized in SI. The Landau coefficients of the FE-HfO_2 thin film have not been studied in detail yet, but they could be varied depending on the film composition (Hf:Zr ratio), dopant concentration or even the process conditions that influence the microstructure [26,27]. Therefore, in this paper, the Landau coefficients at room temperature and δ were used as the fitting parameters to reproduce the discharging curves in Figure 4.5f for 5, 7, and 10 nm-thick AO/HZO bilayers based on the formula above and SI. The use of Equation (4.1) and (4.2) unlike to the previous paper is to further reflect the polycrystalline character of the HZO material on the theory, by which the fitted

coefficients appeared to be as relevant as possible with the real property of HZO material used in this work. Meanwhile, the existence of σ_i induces the lateral shift of the voltage region, where nonlinear increase of the slope begins to appear in the charge density-voltage plot, irrespective of the aforementioned fitting parameters.

The depolarization field by the isotropic average method can be expressed as follows.

$$E_{dep} = \frac{\sigma_i - \frac{1}{2}P_s}{\varepsilon_0 l_f}\left(\frac{3}{4}\cdot\frac{\varepsilon_{\Sigma/3}}{l_f} + \frac{\varepsilon_d}{l_d}\right)^{-1} \tag{4.3}$$

Similarly, the internal voltage can be expressed as follows.

$$V_{int} = \frac{\sigma_i - \frac{1}{2}P_s}{\varepsilon_0}\left(\frac{3}{4}\cdot\frac{\varepsilon_{\Sigma/3}}{l_f} + \frac{\varepsilon_d}{l_d}\right)^{-1} \tag{4.4}$$

Charge density-voltage plot by the previous report of Kim et al. can be modified for the random-orientational ferroelectric material as shown below.

$$\mathrm{D}(P_s) = D_{DE} = D_{FE} - \sigma_i = \frac{3}{2}\varepsilon_0\varepsilon_{\Sigma/3}\frac{\partial F_{f,0}}{\partial P_s} + \frac{1}{2}P_s - \sigma_i \tag{4.5}$$

$$\mathrm{V}(P_s) = l_f E_{ext,f} + l_d E_{ext,d} = \left(l_f + \frac{3}{4}\cdot\varepsilon_{\Sigma/3}\frac{l_d}{\varepsilon_d}\right)E_{ext,f} = \left(l_f + \frac{3}{4}\cdot\varepsilon_{\Sigma/3}\frac{l_d}{\varepsilon_d}\right)\left(2\frac{\partial F_{f,0}}{\partial P_s} - E_{dep}\right) \tag{4.6}$$

The charge density measured in the oscilloscope is the change in the electric displacement.

$$Q(V) = D_{tot}(V) - D_{tot}(V = 0) \quad (4.7)$$

The table (4.1) shows the parameters used in the simulation. $\varepsilon_{\Sigma/3}$ is obtained by multiplying ~24 measured from the non-switching capacitance density at 0V by 4/3 due to the isotropic average calculation, which is almost in agreement with the average dielectric constant of the Zr-rich (Hf,Zr)O_2 material reported by the first principle result. 8.9 was used for ε_d according to the literature, and the Landau coefficient and δ were fitted with the identical values for all AO thicknesses. Figure 4.7 shows the changes of fitted lines for the different simulation parameters in the 10nm-thick AO/HZO thin films. The free energy potentials for the different P_r values can be observed in Figure 4.7a, and the corresponding charge density change is plotted in Figure 4.7b. When the P_r value is lowered, the critical thickness for NC transition is shown to increase with the appearance of the hysteretic S-curve. This is because the depolarization field that destabilizes the ferroelectric state becomes smaller as P_r is lowered as shown in equation (4.3). Figure 4.7b and c show the simulated free energy potential and the charge density curves, respectively, with the different activation energies. The critical thickness for NC transition is shown to increase as the activation energy increases due to more stabilization of the FE state, which is a well-known behavior. The result of Figure 4.8 possibly suggests a different combination of the Landau coefficients which may simulate the nonlinear charge density response of the experimental NC region of the 10nm-thick AO/HZO thin films. Figure 4.8 shows the results using $1.4E_a$ and $1.2P_r$, which potentially transform

the nonlinear slope in an opposite way, compared to the fitted line. Although the nonlinear region is well simulated, it can be observed that the linear charge density response in the low voltage region is deviated from the experimental results.

From the magnitude of the lateral shifts of the nonlinear curves in the Q-V plots, the σ_i could be identified as -0.151, -0.123, -0.119 C m^{-2} for the 5, 7, and 10 nm-thick AO/HZO bilayers, respectively, which are almost the same magnitude as the maximum P_{sw} (~0.14 C m^{-2} at ~1.1 MV cm^{-1}) in Figure 4.3a. This indicates that the spontaneous polarization in the AO/HZO bilayer is mostly compensated by σ_i in the pristine state, which corroborates the static P-V and C-V measurement results shown in Figure 4.3. The fitted Landau coefficients (α, β, and γ) generate the P_r value of the film as ~0.14 C m^{-2}, which is also in agreement with the maximum P_{sw} value in Figure 4.3a. It should be noted that it is much smaller than P_r of ~0.25 C m^{-2} obtained from the ideal random orientation assumption with the homogeneous o-phase [24]. This is because the phases other than the ferroelectric o-phase, especially the tetragonal phase with a relatively small energy difference from the ferroelectric o-phase due to the structural similarity, are generally formed particularly near the interface regions in the Zr-rich polycrystalline (Hf,Zr)O_2 thin films [28]. This decreases the apparent P_r value of the HZO layer. A charged point defect, such as oxygen vacancy in the polycrystalline ferroelectric doped HfO_2 capacitor, is also known to decrease the P_r value by polarization pinning mechanism in the various polycrystalline ferroelectric thin films [21].

Figure 4.9 shows a theoretical analysis on the NC operation of the AO/HZO bilayers shown in Figure 4.5f. The discharge density in Figure 4.5f is identical with the change of electric displacement, which consisted of a linear contribution by the background dielectric constant ($\varepsilon_{\Sigma/3}$) and a nonlinear contribution by the P_s switching as shown in Equation (4.1). In Figure 4.9a, the nonlinear P_s change in the HZO thin film (dotted lines) was plotted separately from the change of the total discharge density (solid lines), which is the same as the dotted line in Figure 4.5f. P_s of the HZO thin film was represented as $(1/2)P_s$ since only the interface-normal component, which means switchable part of the total P_s, contributes to the experimental results, as shown in Equation (4.1). P_s contribution from the non-switching fraction, denoted as δ, should not be included. When the applied voltage is zero, the $(1/2)P_s$ coincided at ~-0.14 C m^{-2} for the 5-10nm-thick AO/HZO bilayers. However, when the sufficiently large external voltage is applied, the nonlinear increase of the $(1/2)P_s$ can be observed, as expected. It should be noted that this P_s switching is almost reversible, meaning that the P_s switched back to the initial state (~-0.14 C m^{-2}) when the voltage was removed, which is in a stark contrast to the conventional ferroelectric switching. This is due to the involvement of the very insulating AO layer, which inhibits the charge injection to change σ_i. As long as σ_i retains the initial value, P_s recovers its pristine value, which coincides with the NC effect of this bilayer structure.

It should also be noted that, however, the switched $(1/2)P_s$ could hardly reach +0.14 C m^{-2}, which is the saturated positive $(1/2)P_s$ value, even at a very high positive applied voltage. This is due to the voltage partake effect of the AO layer, which

became more significant as the AO thickness increased, i.e., the achievable +(1/2)P_s value for the 5nm AO/HZO bilayer was almost +0.14 C m^{-2}, but it was +0.08 C m^{-2} even at +20V in the case of the 10nm AO/HZO sample. Actually, only the values much lower than these maxima could be achieved from the experiment due to a large increase in the leakage current. This eventually lead to the hard breakdown at voltages higher than the values as indicated by the arrows in Figure 4.9a, at which the maximum switched (1/2)P_s was -0.07, 0.02 C m^{-2}, and 0.05 C m^{-2} for the AO thickness of 5, 7, and 10 nm, respectively. If there were no breakdown, the maximum switched (1/2)P_s should be 0.14 C m^{-2} for all AO thicknesses at sufficiently high voltages.

Figure 4.9b shows the variations in the internal voltage across the DE layer (ΔV_{int}; dotted line) and the corresponding charge density (ΔQ_{NC}; solid line) as a function of the applied voltage for the 5-10 nm-thick AO/HZO thin films. If there was no contribution of the P_s switching during the voltage increase, V_{int} must increase gradually as the AO thickness increases where the sample with the thickest AO film shows the highest value, which is accompanied with the increasing depolarization field and voltage across the HZO layer. However, as P_s switches from the imprinted pristine state as in this work with the switched ferroelectric charge being uncompensated, the ΔV_{int} increase was suppressed up to the voltage indicated by the arrows in Figure 4.9a. As the switching voltage increased with the AO thickness, the ΔV_{int} increase was also retarded making the value almost identical at the highest applied voltage of 20 V shown by the dotted lines in Figure 4.9b. Also

shown in the same figure is ΔQ_{NC} which can be readily calculated from the estimated ΔV_{int} using Equation (4.8) below.

$$\Delta Q_{NC} = (1 - \delta) C_{DE} \cdot \Delta V_{int} \tag{4.8}$$

, where $(1 - \delta)$ is the domain fraction aligned opposite to the applied voltage and C_{DE} represents the capacitance of the AO layer. Here, ΔQ_{NC} represents the additionally induced charge density by the (reversible) P_s switching, which was as high as ~0.085 C m^{-2} for the 5 nm-thick AO/HZO case, but decreased to ~0.04 C m^{-2} for the 10 nm-thick AO/HZO case at 20 V. While the maximum switchable P_s decreased from ~0.28 C m^{-2} for the 5 nm-thick AO/HZO to ~0.22 C m^{-2} for the 10 nm-thick AO/HZO (~21% decrease), the ΔQ_{NC} decrease was more significant (~53%). This was due to the concurrent decrease in C_{DE} with the increasing AO thickness. It should be reminded that all these calculations were based on the assumption that σ_i is invariant upon the voltage application, which could be confirmed from the data in Figure 4.9c.

From these estimations, the total capacitance of the AO/HZO stacked layers can be calculated as a function of the applied voltage by differentiating the charge density data in Figure 4.9a with respect to the applied voltage (lines in Figure 4.9c), which can be compared with the experimentally determined values (symbols in Figure 4.9c), which could be achieved by differentiating the experimental data in Figure 4.5f. Although the peak values of the calculated capacitance could not be precisely

reproduced by the experiments, due to the involvement of large leakage current and accompanying possible breakdown, the experimental data in the low voltage region precisely follow the calculated curves, demonstrating the accuracy of the modeling. The most critical point is the voltage regions where the estimated capacitance values of the bilayer structures are higher than that of the single layer AO with each thickness (flat lines). This is a direct experimental proof that the (transient) capacitance boosting effect was induced by the suggested NC effect of the ferroelectric HZO film, although it has a polycrystalline structure even with the non-negligible incorporation of non-ferroelectric phases. In such pulse-wise device operation, the presence of non-ferroelectric phase is irrelevant to the involvement of such transient NC effect. Of course, if the portion of the non-ferroelectric phase is too high, the paraelectric-like behavior of the HZO film could dominate the (small) contribution of the P_s switching, making such effect even unobservable. Therefore, confirming the high quality of the ferroelectricity is still of crucial important even for the polycrystalline film.

The reliability of the transient NC operation in the AO/HZO bilayer thin film was examined in Figure 4.10. Figure 4.10a shows the charge density-voltage curve of the ~7 nm-thick AO/HZO capacitor when the applied voltage was increased to 13 V. In the high voltage region > ~12 V, the Q_{res} gradually increased due to the increased charge loss by the leakage current through the AO layer, which was also observed in the previous report [18]. Within this voltage range, the hysteretic (dis-) charge density-voltage behavior can be observed when voltage sweep direction was alternated as shown in Figure 4.10b. The inset shows their corresponding capacitance density changes. There was an increased discharge density between ~8 V and ~12 V

during the voltage sweeping down (dark yellow symbols) and subsequent voltage sweeping up (grey symbols) steps. The precisely overlapped responses during the voltage sweeping down and subsequent voltage sweeping up indicated that a certain permanent change has been occurred during the first sweeping up step, especially at the very high voltage (~ 13 V). Such a change is believed to be a damage of the AO layer, resulting in an increase in the leakage current through that layer. A shift of the discharging curve into the low voltage direction cannot be ascribed to the change (decrease) in σ_i due to the opposite charge injection at ~13V. This is because the entire curve (mostly from ~ 8V up to 13 V) must be shifted towards the low voltage region if the σ_i has been decreased, which was obviously not the case. It can be assumed that the resistance of the AO layer was decreased by the damaging effect (soft breakdown or resistance degradation) at ~ 13V during the first sweeping up step. Then, the voltage applied to the HZO layer must be increased, making the charging-discharging responses enhanced. This made the charge responses during the subsequent sweeping down and up increase at a voltage higher than ~ 8V. It should be noted that the charge response at V > ~12 V was already enhanced during the first sweeping up step, so there must be no further increase in the charge/discharge responses in the subsequent steps.

Under such high voltage operation, the device was susceptible to the early breakdown as shown in Figure 4.10c. Only after 50 switching cycles, the device showed a significant increase in Q_{res} by the dielectric breakdown of the bilayer. A slight decrease in the charge/discharge density in Figure 4.10c up to 50 cycles could be explained by the slight increase in the permanently switched domain fraction

(denoted as δ in Equation (4.2)) during the repeated tests. In contrast, when the bilayer capacitor is operated in the region where the residual charge does not vary (9, 11, and 17 V for the 5, 7, and 10 nm AO, respectively), no hysteresis formation can be observed in the charge density-voltage plot as shown in the inset of Figure 4.10c. In addition, the stable charging/discharging operations of more than 10^3 cycles were confirmed for the 7 nm- and 10 nm-thick AO/HZO capacitors with broad voltage ranges to cover the NC operation regions as shown in Figure 4.10d. Also, the degradation by domain pinning of HZO layer due to charged defects could not be observed. It can be understood that the Q_{res} remained negligible for all the switching cycles for both samples, suggesting the robustness of the device against the charge leakage.

4.4. Summary

The transient negative capacitance (NC) effect in an amorphous-Al_2O_3/polycrystalline-(Hf,Zr)O_2 (DE/FE) bilayer capacitor on the CMOS-compatible TiN electrode was reported in detail. The post-deposition annealed $Hf_{0.3}Zr_{0.7}O_2$ thin film showed the feasible ferroelectric behavior with the maximum $2P_r$ (~0.21 C m^{-2}) to observe the transient NC effect with no evolution of parasitic (non-ferroelectric) monoclinic phase with the highly insulating property of Al_2O_3 layer. During the pulse-wise capacitance measurement, the inflow of the compensating charge toward the $Hf_{0.3}Zr_{0.7}O_2$ interface was effectively suppressed with the highly insulating Al_2O_3 layer, and thus, the NC state of the spontaneous polarization (P_s) could be observed transiently. The capacitance enhancement due to the transient NC effect was observed in the 5-10nm-thick AO/HZO bilayer capacitors with a wide applied voltage range, and it was well simulated based on the Landau-Ginzburg-Devonshire theory and the related electrostatic calculations. It was found that the interface charge density (σ_i) between the Al_2O_3 and the $Hf_{0.3}Zr_{0.7}O_2$ layers ranged from -0.12 C m^{-2} to -0.15 C m^{-2} for the 5-10 nm-thick Al_2O_3/$Hf_{0.3}Zr_{0.7}O_2$ bilayers, which is comparable to the maximum P_{sw} (~0.14 C m^{-2}) of the $Hf_{0.3}Zr_{0.7}O_2$ layer, suggesting that that the P_s of the HZO layer is mostly compensated by σ_i in the pristine state. It was also revealed that the additional charge density induced by the NC effect is highly dependent on the capacitance of the dielectric layer whereas the change in the internal voltage across the dielectric layer is almost insignificant. For the increase of the charge density, the homogeneous ferroelectric phase formation in the FE layer is necessary.

The stable transient NC operation was confirmed in the voltage range where the charge injection through the DE layer does not occur, and in this condition, nonhysteretic and stable charging/discharging operations over 10^3 times were confirmed.

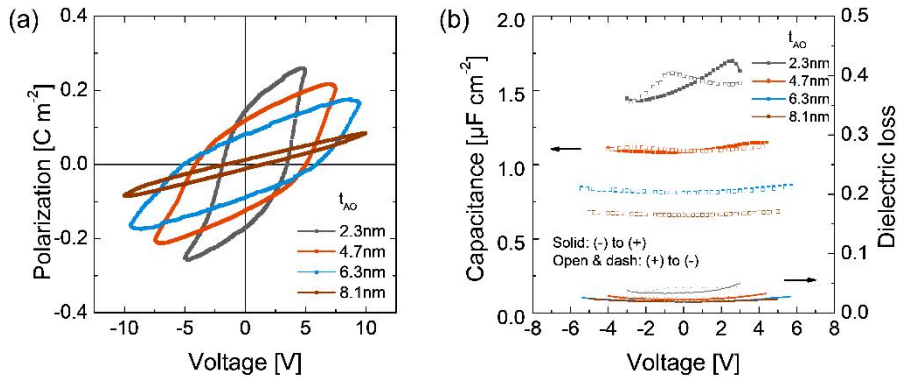

Figure 4.1 (a) The polarization – voltage curves and (b) low-frequency AC capacitance – voltage curves for the 2-8 nm-thick Al_2O_3 / $Hf_{0.5}Zr_{0.5}O_2$ bilayer thin films crystallized under the post-metallization (Pt) annealing condition.

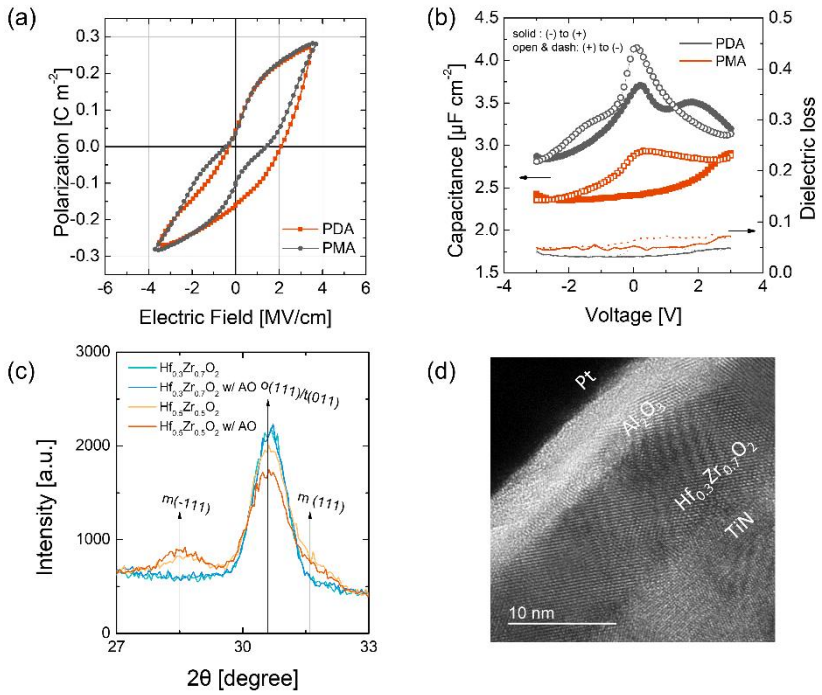

Figure 4.2 (a) The polarization – electric field curves and (b) low-frequency capacitance – voltage curves for the ~10nm-thick $Hf_{0.3}Zr_{0.7}O_2$ thin films crystallized under the conditions of the post-deposition annealing and the post-metallization annealing. (c) The glancing angle X-ray diffraction results for the ~10nm-thick $Hf_{0.3}Zr_{0.7}O_2$ and $Hf_{0.5}Zr_{0.5}O_2$ thin films before and after ~10nm-thick Al_2O_3 deposition. (d) The cross-sectional high-resolution transmission electron microscopy of the ~7 nm-thick Al_2O_3 / ~10nm-thick $Hf_{0.3}Zr_{0.7}O_2$ thin film.

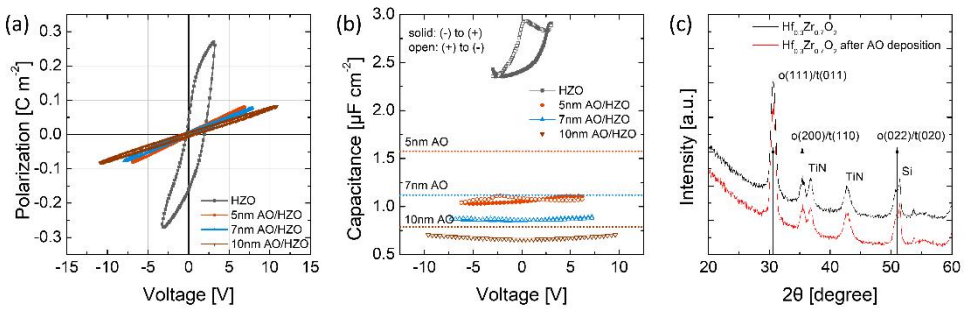

Figure 4.3 (a) Polarization – voltage curves and (b) low-frequency AC capacitance – voltage curves for the ~10nm-thick $Hf_{0.3}Zr_{0.7}O_2$ thin films and the 5-10nm-thick Al_2O_3 / ~10nm-thick $Hf_{0.3}Zr_{0.7}O_2$ bilayer thin films. The horizontal dotted line in (b) indicates the theoretical AO single layer capacitance for each AO thickness. (c) Glancing-angle X-ray diffraction of the ~10nm-thick $Hf_{0.3}Zr_{0.7}O_2$ thin films after crystallization and Al_2O_3 deposition.

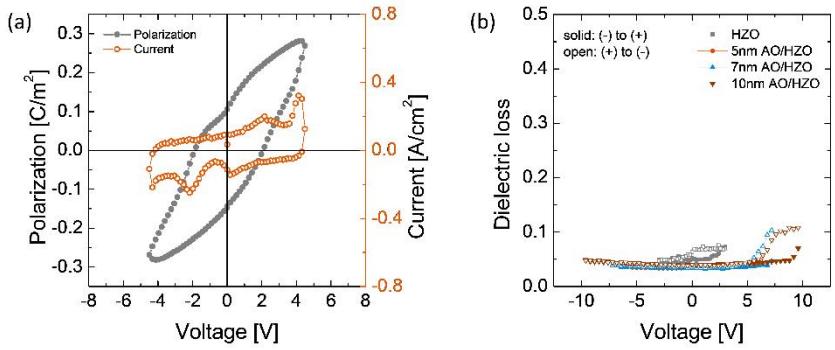

Figure 4.4 (a) The polarization – voltage curves for the ~10nm-thick $Hf_{0.3}Zr_{0.7}O_2$ thin film under the different external voltage magnitudes. (b) The dielectric loss – voltage curves for the capacitance – voltage curves of Figure 4.3b.

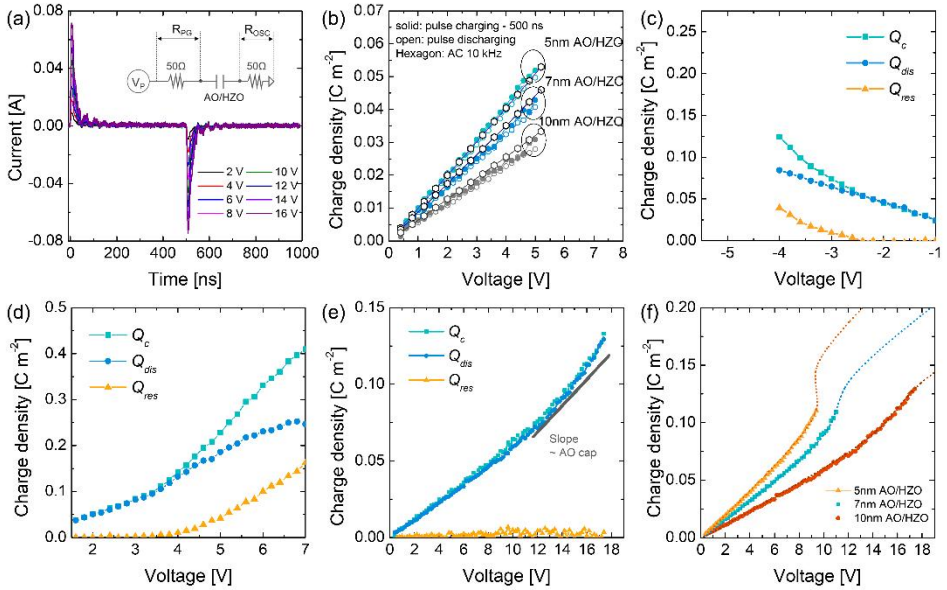

Figure 4.5 (a) Capacitor charging and discharging current of the 10nm-thick Al_2O_3 / $Hf_{0.3}Zr_{0.7}O_2$ bilayer capacitor and equivalent circuit diagram for the pulse charging system (inset). (b) Capacitor charge density – voltage curves obtained from the pulse charging system and the AC capacitance measurement system with 10kHz frequency for the Al_2O_3 / $Hf_{0.3}Zr_{0.7}O_2$ bilayer capacitors. Stored charge (Q_c), released charge (Q_{dis}), and the residual charge (Q_{res}) for (c), (d) the ~10nm-thick $Hf_{0.3}Zr_{0.7}O_2$ thin film and (e) the 10nm-thick Al_2O_3 / $Hf_{0.3}Zr_{0.7}O_2$ bilayer thin films. (f) discharge density – voltage plot for the 5-10nm-thick Al_2O_3 / $Hf_{0.3}Zr_{0.7}O_2$ bilayer thin films.

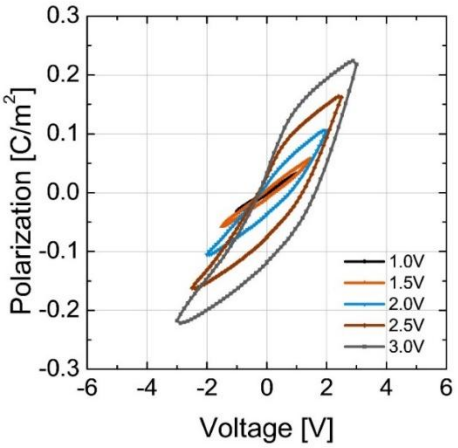

Figure 4.6 The polarization – voltage curves for the ~10nm-thick $Hf_{0.3}Zr_{0.7}O_2$ thin film under the different external voltage magnitudes.

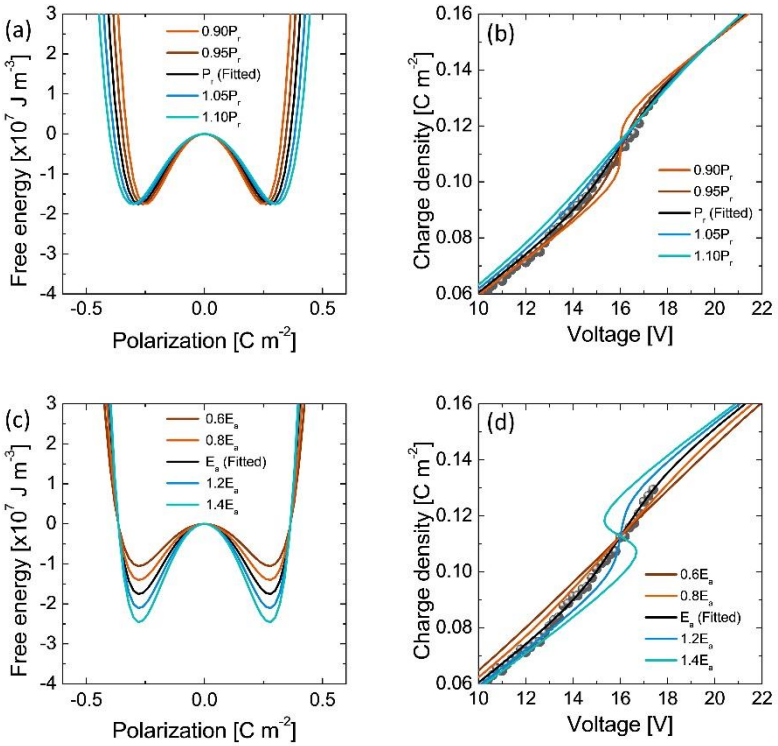

Figure 4.7 The exemplary change of Landau coefficients based on the fitted (a) P_r and (c) E_a, and (b), (d) their corresponding charges in the charge density curve for the ~10nm-thick Al_2O_3 / $Hf_{0.3}Zr_{0.7}O_2$ bilayer thin film.

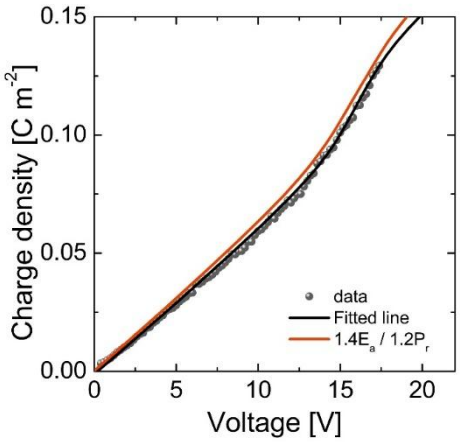

Figure 4.8 The measured (dot) and the fitted (black line) discharge density of the ~10nm-thick Al_2O_3 / $Hf_{0.3}Zr_{0.7}O_2$ bilayer thin film, and the fitting example (red line) using different Landau coefficients.

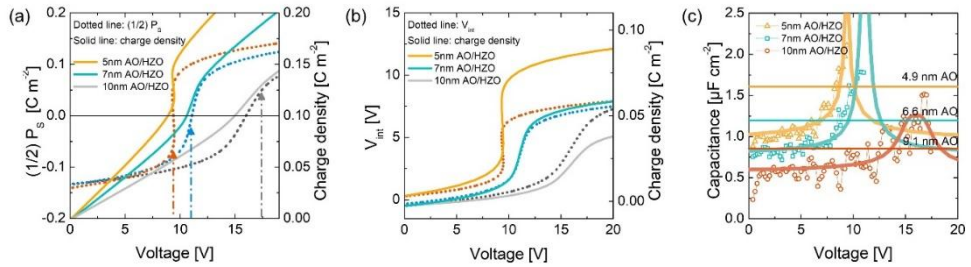

Figure 4.9 (a) The change of spontaneous polarization (left) and the discharge density (right) according to the bias voltage; the vertical arrows indicate the change of spontaneous polarization at the maximum applicable bias voltage. (b) The internal voltage (left) and discharge density originated from the negative capacitance effect (right) for the Al_2O_3 / $Hf_{0.3}Zr_{0.7}O_2$ bilayer thin films. (c) the measured (dot), simulated (bold line), and the respective AO single layer (horizontal line) capacitances for the Al_2O_3 / $Hf_{0.3}Zr_{0.7}O_2$ bilayer thin films.

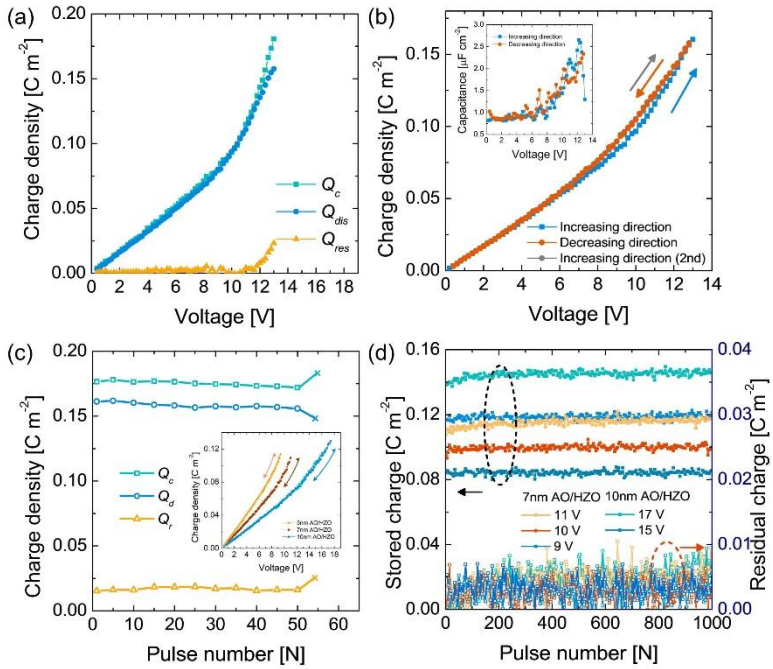

Figure 4.10 (a) The stored charge (Q_c), released charge (Q_{dis}), and residual charge (Q_{res}) of the 7nm-thick Al_2O_3 / $Hf_{0.3}Zr_{0.7}O_2$ bilayer thin film with the maximum bias voltage of 13V. (b) The hysteretic discharge density curve and capacitance density (inset) of the 7nm-thick Al_2O_3 / $Hf_{0.3}Zr_{0.7}O_2$ bilayer thin film with the change of bias direction. (c) The charge density changes with the repetitive bias application in the 7nm-thick Al_2O_3 / $Hf_{0.3}Zr_{0.7}O_2$ bilayer thin film, and the non-hysteretic discharge density curve (inset) of the 5-10nm-thick Al_2O_3 / $Hf_{0.3}Zr_{0.7}O_2$ bilayer thin film with increasing and decreasing bias directions. (d) The stored charge (left), and residual charge (right) of the 7 and 10nm-thick Al_2O_3 / $Hf_{0.3}Zr_{0.7}O_2$ bilayer thin films as a function of pulse number.

AO Thickness	5nm	7nm	10nm
$\varepsilon_{\Sigma/3}$ / ε_d		31.94 / 8.9	
α / β / γ		-7.0E08 / 5.37E08 / 1.13E11	
δ		0.3	
σ_i [C m^{-2}]	-0.151	-0.123	-0.119

Table 4.1 The simulation parameters of the electrostatic calculation based on the Landau-Ginzburg-Devonshire model.

4.5. Bibliography

[1] S. Salahuddin, S. Datta, *Nano Lett*., 8, 405-410 (2008).

[2] V. V. Zhirnov, R. K. Cavin, *Nat. Nanotechnol*., 3, 77-78 (2008).

[3] C. S. Hwang, *Adv. Electron. Mater*., 1, 1400056 (2015).

[4] A. I. Khan, K. Chatterjee, B. Wang, S. Drapcho, L. You, C. Serrao, S. R. Bakaul, R. Ramesh, S. Salahuddin, *Nat. Mater*., 14, 182-186 (2015).

[5] S. Kasamatsu, S. Watanabe, C. S. Hwang, S. Han, *Adv. Mater*., 28, 335-340 (2016).

[6] Y. J. Kim, H. W. Park, S. D. Hyun, H. J. Kim, K. D. Kim, Y. H. Lee, T. Moon, Y. B. Lee, M. H. Park, C. S. Hwang, *Nano Lett*., 17, 7796-7802 (2017).

[7] A. I. Khan, D. Bhowmik, P. Yu, S. J. Kim, X. Pan, R. Ramesh, S. Salahuddin, *Appl. Phys. Lett*., 99, 113501 (2011).

[8] D. J. R. Appleby, N. K. Ponon, K. S. K. Kwa, B. Zou, P. K. Petrov, T. Wang, N. M. Alford, A. O'Neill, *Nano Lett*., 14, 3864-3868 (2014).

[9] W. Gao, A. I. Khan, X. Marti, C. Nelson, C. Serrao, J. Ravichandran, R. Ramesh, S. Salahuddin, *Nano Lett*., 14, 5814-5819 (2014).

[10] A. L. Roytburd, S. Zhong, S. P. Alpay, *Appl. Phys. Lett*., 87, 092902 (2005).

[11] Y. J. Kim, M. H. Park, W. Jeon, H. J. Kim, T. Moon, Y. H. Lee, K. D. Kim, S. D. Hyun, C. S. Hwang, *J. Appl. Phys*., 118, 224105 (2015).

[12] Y. J. Kim, M. H. Park, Y. H. Lee, H. J. Kim, W. Jeon, T. Moon, K. D. Kim,

D. S. Jeong, H. Yamada, C. S. Hwang, *Sci. Rep.*, 6, 19039 (2016).

[13] A. Rusu, G. A. Salvatore, D. Jimenez, A. M. Ionescu, *Proc. IEEE IEDM.*, 395-398 (2010).

[14] G. A. Salvatore, A. Rusu, A. M. Ionescu, *Appl. Phys. Lett.*, 100, 163504 (2012).

[15] Y. G. Xiao, M. H. Tang, J. C. Li, C. P. Cheng, B. Jiang, H. Q. Cai, Z. H. Tang, X. S. Lv, X. C. Gu, *Appl. Phys. Lett.*, 100, 083508 (2012).

[16] Y. G. Xiao, Z. J. Chen, M. H. Tang, Z. H. Tang, S. A. Yan, J. C. Li, X. C. Gu, Y. C. Zhou, X. P. Ouyang, *Appl. Phys. Lett.*, 101, 253511 (2012).

[17] H. W. Park, J. Roh, Y. B. Lee, C. S. Hwang, *Adv. Mater.* accepted.

[18] Y. J. Kim, H. Yamada, T. Moon, Y. J. Kwon, C. H. An, H. J. Kim, K. D. Kim, Y. H. Lee, S. D. Hyun, M. H. Park, C. S. Hwang, *Nano Lett.*, 16, 4375-4381 (2016).

[19] A. Q. Jiang, H. J. Lee, G. H. Kim, C. S. Hwang, *Adv. Mater.*, 21, 2870−2875 (2009).

[20] J. Müller, T. S. Böscke, U. Schröder, S. Müller, D. Bräuhaus, U. Böttger, L. Frey, T. Mikolajick, *Nano Lett.*, 12, 4318 (2012).

[21] M. H. Park, Y. H. Lee, H. J. Kim, Y. J. Kim, T. Moon, K. D. Kim, J. Müller, A. Kersch, U. Schröder, T. Mikolajick, C. S. Hwang, *Adv. Mater.*, 27, 1811 (2015).

[22] K. M. Rabe, C. H. Ahn, J.-M. Triscone, *Physics of Ferroelectrics: A*

Modern Perspective, Springer, New York (2007).

[23] M. J. Biercuk, D. J. Monsma, C. M. Marcus, J. S. Becker, R. G. Gordon, *Appl. Phys. Lett.*, 83, 2405 (2003).

[24] R. Materlik, C. Künneth, A. Kersch, *Appl. Phys. Lett.*, 117, 134109 (2015).

[25] S. E. Reyes-Lillo, K. F. Garrity, K. M. Rabe, *Phy. Rev. B*, , 90, 140103(R) (2014).

[26] K. D. Kim, Y. H. Lee, T. Gwon, Y. J. Kim, H. J. Kim, T. Moon, S. D. Hyun, H. W. Park, M. H. Park, C. S. Hwang, *Nano Energy*, 390-399 (2017).

[27] M. H. Park, C.-C. Chung, T. Schenk, C. Richter, M. Hoffmann, S. Wirth, J. L. Jones, T. Mikolajick, U. Schroeder, *Adv. Electron. Mater.*, 4, 1700489 (2018).

[28] M. H. Park, H. J. Kim, Y. J. Kim, Y. H. Lee, T. Moon, K. D. Kim, S. D. Hyun, F. Fengler, U. Schroeder, C. S. Hwang, *ACS Appl. Mater. Interfaces*, 8, 15466-15475 (2016).

5. Conclusion

In this dissertation, the induction of reversible polarization switching in HfO_2-ZrO_2 thin films and their energy storage and negative capacitance applications were explored in detail. The (field-induced) ferroelectric HfO_2-ZrO_2 thin film now attracts a great interest especially as a solution to realize the high-power energy storage device or the future miniaturized semiconductor memory device. At 2014, the field-induced ferroelectric HfO_2-ZrO_2 thin film were suggested to be used as an electrostatic supercapacitor, one of solid-state energy storage devices. Also, it showed the high energy storage density up to ~46 J/cm^3 at ~9nm-thick $Hf_{0.3}Zr_{0.7}O_2$ thin film. However, the large energy storage density drastically decreased to ~21 J/cm^3 when the film thickness increased to ~19 nm, which was due to the low-k monoclinic phase fraction increased in the thin film. It was considered the major obstacle to increase the total energy storage quantity based on the field-induced ferroelectric HfO_2-ZrO_2 capacitors because large enough thickness ratio between the dielectric and electrode layers is required even though it was incorporated as 3D-structure by atomic layer deposition method. This work considered the monoclinic phase formation can be reduced when the in-situ (partial) crystallization during the atomic layer deposition is suppressed. It is because the absence of top encapsulation effect during the in-situ crystallization can easily allow the transformation to stable monoclinic phase. Considering the in-situ crystallization is a thermally-activated process, the atomic layer deposition temperature of HfO_2-ZrO_2 thin film was lowered. During the change of deposition

temperature, the carbon and nitrogen dopants originated from the precursor-ligand incorporated in a thin film at a low deposition temperature. In combination with grain size decrease, the polymorphism of $Hf_{0.5}Zr_{0.5}O_2$ thin film changed from ferroelectric to field-induced ferroelectric crystal structure. The field-induced ferroelectricity by reversible polarization switching operation enables the thin film to represent large recoverable energy density with reduced energy loss. The $Hf_{0.5}Zr_{0.5}O_2$ thin film deposited at 210 ºC showed improved resistance to degradation by monoclinic phase involvement up to ~40 nm compared to the previously-reported $Hf_{0.3}Zr_{0.7}O_2$ thin films. The maximum film thickness of ~40 nm is large enough thickness when considering the incorporation in 3-D structure, but the insufficient energy storage density compared to other methods still hinders direct adaptation of this material. The hybrid energy storage system with electrochemical supercapacitor can be viable solution.

The another method for inducing reversible polarization switching studied in this work is to exploit the depolarization field generated by the inserted dielectric layer between ferroelectric and electrode layers. The ferroelectric/dielectric bilayer capacitor can represent the capacitance boosting due to the negative capacitance effect of ferroelectric material, where the bilayer capacitance density can be larger than the capacitance density of the constituent dielectric layer in the bilayer structure. The reversible polarization switching induced by incipient depolarization field facilitate the increase of (dis-) charged charge density. However, to date, the NC effect in ferroelectric/dielectric bilayer capacitors were reported only in epitaxial ferroelectric thin films based on perovskite-crystal structures, such as $Pb(Zr,Ti)O_3$

and $BaTiO_3$, which limits the use of such effect in current complementary metal oxide semiconductor technology. Therefore, this work studied on the (transient) NC effect in amorphous-Al_2O_3/polycrystalline-$Hf_{0.3}Zr_{0.7}O_2$ bilayer systems prepared using atomic layer deposition. To reduce thermal budget of amorphous-Al_2O_3 layer, the crystallization process of HfO_2-ZrO_2 thin film was conducted in post-deposition annealing process, and in this crystallization thermal treatment, the Zr ratio need to be increased than 50 at% to reduce the low-k monoclinic phase fraction. The absence of top encapsulation effect facilitates the crystallization to the desired ferroelectric orthorhombic phase rather than field-induced ferroelectric tetragonal phase. Capacitance enhancement is observed in a wide voltage range in 5–10 nm thick Al_2O_3/$Hf_{0.3}Zr_{0.7}O_2$ bilayer thin films. It is found that the capacitance of the dielectric layer plays critical role in the determination of additional charge density induced by the NC effect. The appearance of interface trap charge between Al_2O_3 and $Hf_{0.3}Zr_{0.7}O_2$ layers hindered the low voltage operation of NC effect, which needs to be reduced for static NC operation in future studies.

Abstract (in Korean)

에너지 및 메모리 소자 응용을 위한 HfO_2-ZrO_2 고용체 박막의 가역적 자발 분극 스위칭 현상 유도 연구

도핑한 HfO_2 및 HfO_2-ZrO_2 고용체 박막에서 나타나는 강유전성과 전계 유도 강유전성은 2011년 처음 보고된 이후 집중적으로 연구 되어왔다. 이러한 박막들은 기존 페로브스카이트 기반의 강유전체 박막과 비교할 때 훨씬 큰 밴드 갭 에너지 (~5.5 eV) 및 Si-compatibility 등을 가져 미래 반도체 소자로 사용되기에 뚜렷한 이점들을 나타내었다. 반면, 기존의 연구들은 주로 전극-강유전체-전극 또는 전극-강유전체-(상유전체)-반도체 전극 구조 상에서 비가역적 분극 스위칭에 기반한 강유전체 물성과 이와 관련된 비휘발성 메모리 소자 측면에 주목하였으며, 특정 조건 하에서 HfO_2-ZrO_2 박막 상에 유도될 수 있는 가역적 분극 스위칭 현상에 대해서는 체계적으로 연구가 되지 않았다. 가역적 분극 스위칭은 인가한 전계가 제거되어도 스위칭된 상태가 유지되는 일반적인 강유전체 커패시터와 반대로, 인가한 전계가 제거될 때 스위칭된 자발 분극이 초기 분극 상태로 되돌아오는 특성을 의미한다. 이러한 분극 스위칭 특성을 보이는 강유전체 박막은 외부 전압이 없는 상태에서 어떤 메모리 상태도 유지할 수 없

기 때문에 비휘발성 메모리 소자로써는 사용되기 힘든 반면, 자발 분극 스위칭에 의해 유도되는 큰 커패시턴스 변화를 통해 에너지 및 음의 커패시턴스 (negative capacitance; NC) 소자로써 유망한 특성들을 나타낼 수 있다. 따라서 본 연구는 HfO_2-ZrO_2 박막 상에서 챕터 3과 4에서 제시되는 두 가지 다른 방법을 이용하여 가역적 분극 스위칭을 유도하고, 이를 각각 에너지 및 NC 메모리 소자로써 활용한 내용에 대해 다루었다.

챕터 3에서는 무극성의 정방(tetragonal) 상을 안정화하는 방법을 통해 가역적 분극 스위칭을 유도하고, 이를 통해 MIM 커패시터의 정전기적 에너지 저장 소자 응용을 연구하였다. HfO_2-ZrO_2 박막 내에서는 정방 상이 안정화될 때 인가한 전계에 의해 가역적으로 극성의 사방정계 (orthorhombic) 상으로 상전이가 가능하다. 이는 P-E 커브 상에서 큰 P_{max}와 작은 P_r을 갖는 이중-히스테리시스를 나타나게 하는데, 이는 정전기적 슈퍼커패시터 소자에 적합한 특성이다. 그러나 현재까지 HfO_2-ZrO_2 박막에서 나타나는 큰 에너지 저장 특성은 ~10 nm 이상의 두꺼운 두께에서 낮은 유전율의 규모를 증가시키는 데 단사정(monoclinic) 상의 생성으로 인한 스케일업의 장애를 가져왔다. 단사정 상의 생성이 원자층 증착법 (atomic layer deposition; ALD) 과정 중 부분적인 insitu-결정화 현상과 큰 관련이 있음을 고려하여 낮은 ALD 온도에서의 $Hf_{0.5}Zr_{0.5}O_2$ 박막 증착과 이를 이용한 에너지 저장 특성을 체계적으로 연구하였다. 낮은 증착 온도에서 탄소와 질소 도펀트 및 그레인 크기의 변화에 의해 $Hf_{0.5}Zr_{0.5}O_2$ 박막의

결정상은 극성의 사방정 상에서 정방 상으로 변화하였고, 이를 통해 가역적 분극 스위칭을 통한 전계유도 강유전성을 나타낼 수 있었다. 210 ºC에서 증착한 $Hf_{0.5}Zr_{0.5}O_2$ 박막은 기존의 280 ºC에서 증착한 $Hf_{0.3}Zr_{0.7}O_2$ 박막에 비해 ~40 nm 두께까지 더 작은 단사정 상 생성에 의한 열화를 보였고, 이를 통해 개선된 에너지 저장 특성을 나타내었다.

챕터 4에서는 강유전체 층과 전극 층 사이에 유전층 삽입을 통해 탈분극 전계를 유도하고 이를 이용하여 가역적 분극 스위칭을 유도한 연구를 진행하였다. 강유전체 물질의 NC 현상에 의해 가역적 분극 스위칭 중에 나타나는 강유전체/상유전체 이중층의 커패시턴스는 이중층 중에 존재하는 상유전체 층의 단일 커패시턴스보다 커질 수 있다. 이 현상은 (순간적인) NC 현상에 의한 커패시턴스 증폭으로 불리며, 전계 효과 트랜지스터 (field-effect transistor)의 저전력 동작 및 DRAM (dynamic random access memory) 커패시터 소자를 개발하기 위한 목적으로 많은 관심을 끌고 있다. 그러나 현재까지 강유전체/상유전체 이중층 커패시터에서 관찰한 NC 효과는 $Pb(Zr,Ti)O_3$ 및 $BaTiO_3$와 같은 페로브스카이트 결정 구조에 기초한 에피텍셜 (epitaxial) 강유전체 박막에서만 보고가 되었고, 이러한 박막들은 현재 상보형 금속 산화 반도체 (complementary metal oxide semiconductor; CMOS) 공정에 사용되기 어려운 한계를 지닌다. 따라서 본 챕터에서는 ALD를 통해 증착한 비정질-Al_2O_3/다결정-$Hf_{0.3}Zr_{0.7}O_2$ 이중층 구조에서 가역적 분극 스위칭을 유도하고, 이 때 나타나는 순간적인 NC 현상을 연구

하였다. Zr 조성 및 결정화 조건은 순간적인 NC 현상을 뚜렷하게 관찰하기 위해 세밀하게 조정되었다. 5-10 nm 두께의 $Al_2O_3/Hf_{0.3}Zr_{0.7}O_2$ 이중층 박막의 넓은 전압 범위에서 커패시턴스 증폭 현상을 관찰하였다. NC 현상에 의해 추가적으로 유도 가능한 전하 밀도는 적층된 상유전체 층의 커패시턴스에 의해 제한됨을 확인하였다. 상유전체 층을 통한 누설 전류를 억제하는 것이 이중층 커패시터 상에서 히스테리시스 없는 안정적인 충/방전 거동에 필수적인 조건임을 확인하였다.

핵심어: 강유전체, HfO_2-ZrO_2 박막, 정전기적 슈퍼커패시터, 에너지 저장, 커패시턴스 증폭, 음의 커패시턴스, 가역적 분극 스위칭

학번: 2014-21482